Probing the role of Nogo receptor homolog NgR2 in setting up cochlear connectivity

Nare Karagulyan[1,2,3#], Maja Überegger[4#], Yumeng Qi[5#], Norbert Babai[1,2], Florian Hofer[4], Lejo Johnson Chacko[6], Fangfang Wang[5], Maria Luque[6], Rudolf Glueckert[6], Anneliese Schrott-Fischer[6], Yunfeng Hua[5*], Tobias Moser[1,2,3,7*], Christine Bandtlow[4*]

[1]Institute for Auditory Neuroscience, University Medical Center Göttingen, Göttingen, Germany

[2]Auditory Neuroscience and Synaptic Nanophysiology Group, Max Planck Institute for Multidisciplinary Sciences, Göttingen, Germany

[3]Cluster of Excellence "Multiscale Bioimaging of Excitable Cells", 37075 Göttingen, Germany

[4]Institute of Neurobiochemistry, Biocenter, Medical University of Innsbruck, 6020 Innsbruck, Austria

[5]Shanghai Institute of Precision Medicine, Ninth People's Hospital, Shanghai Jiao Tong University School of Medicine, Shanghai 200125, China

[6]Department of Otorhinolaryngology, Medical University of Innsbruck, 6020 Innsbruck, Austria

[7]Department for Hearing, Speech and Voice Disorders, Medical University of Innsbruck, 6020 Innsbruck, Austria

Running title: Expression and function of Nogo receptor homolog NgR2 in the cochlea

[#]equal contribution
*correspondence to
Dr. Christine Bandtlow: christine.bandtlow@i-med.ac.at
Dr. Tobias Moser: tmoser@gwdg.de
Dr. Yunfeng Hua: yunfeng.hua@shsmu.edu.cn

Abstract

Sound encoding depends on the precise and reliable neurotransmission at the afferent synapses between the sensory inner hair cells (IHCs) and spiral ganglion neurons (SGNs). The molecular mechanisms contributing to the formation, as well as interplay between the pre- and postsynaptic components remains largely unclear. Here, we tested the role of the Nogo receptor homolog NgR2 (RTN4rl2) in the development and function of afferent IHC-SGN synapses. Upon deletion of NgR2 in mice (NgR2$^{-/-}$), presynaptic IHC active zones showed enlarged synaptic ribbons and a depolarized shift in the activation of $Ca_V1.3$ Ca^{2+} channels. The postsynaptic densities (PSDs) of SGNs were smaller and deficient of GluA2/3 despite maintained Gria2 mRNA expression in SGNs. Next to synaptically engaged PSDs we observed "orphan" PSDs located away from IHCs. They likely belong to a subset of SGN peripheral neurites that do not contact the IHCs in NgR2$^{-/-}$ cochleae as found by volume electron

microscopy reconstruction of SGN neurites. Auditory brainstem responses of NgR2$^{-/-}$ mice showed increased sound thresholds indicating impaired hearing. Together, these findings suggest that NgR2 contributes to the proper formation and function of auditory afferent synapses and is critical for normal hearing.

Introduction

Hearing relies upon the correct formation and maturation of cochlear afferent synapses between postsynaptic type I spiral ganglion neurons (SGNs) and presynaptic inner hair cells (IHCs; reviewed in Johnson et al., 2019; Bulankina and Moser, 2012; Appler and Goodrich, 2011). In mice, SGN neurites extend and reach IHCs at late embryonic stages (E16.5; Koundakjian, Appler, and Goodrich, 2007), whereby early synaptic contacts are established between the two cells at E18 (Michanski et al., 2019). Developmental changes and maturation of afferent synapses continue until the onset of hearing (p12), with further refinement occurring till the fourth postnatal week (Wong et al., 2014; Liberman and Liberman, 2016; Michanski et al., 2019). In mature cochleae, each IHC receives a contact from 5-30 SGNs, while each SGN contacts only one active zone (AZ) of one IHC in the majority of cases (Meyer and Moser, 2010; Hua et al., 2021).

To this date, multiple mechanisms have been implicated in SGN neurite guidance and establishment of IHC innervation by SGNs, including signaling via EphrinA5-EphA4, Neuropilin2/Semaphorin3F, Semaphorin5B/PlexinA1, Semaphorin3A (Defourny et al., 2013; Coate et al., 2015; Jung et al., 2019; Cantu-Guerra et al., 2023). Less is known about the molecules governing the transsynaptic organization at IHC afferent synapses. Similar to the central conventional synapses, synaptic adhesion proteins such as neurexins and neuroligins have been suggested to play a role in pre- and postsynaptic assemblies (Ramirez et al., 2022; Jukic et al., 2024). Furthermore, the $Ca_V1.3$ extracellular auxiliary subunit $Ca_V\alpha_2\delta_2$ was indicated to be important for proper alignment of presynaptic IHC AZs and postsynaptic densities (PSD) of SGNs (Fell et al., 2015).

Whether Nogo receptors (NgRs) contribute to setting up afferent connectivity in the cochlea remained to be investigated. The Nogo receptor family consists of 3 homologous proteins NgR1-3. NgRs are leucine-rich repeat (LRR) and glycosylphosphatidylinositol (GPI) anchored cell surface receptors (Figure 1A). Their primary role is thought to limit synaptic

63 plasticity and axonal outgrowth as well as to restrict axonal regeneration after injury (reviewed
64 in Mironova and Giger, 2013). While NgR1 and NgR3 are involved in axonal guidance (Vaccaro
65 et al., 2022), NgR2 has been proposed to be important for innervation of the epidermis by
66 dorsal root ganglion neurons (Bäumer et al., 2014). Furthermore, NgRs are suggested to
67 control the number and the development of synapses (Wills et al., 2012) and to play a role in
68 transsynaptic signaling (Wang et al., 2021).

69 Recent single-cell transcriptomic studies of the cochlea detected the expression of
70 NgRs in SGNs and IHCs (Shrestha et al., 2018; Jean et al., 2023). Here, we investigated the role
71 of NgR2 in the cochlea using previously described NgR2 constitutive knock-out mice (NgR2$^{-/-}$,
72 (Wörter et al., 2009). We found NgR2 to be expressed in SGNs and to be required for normal
73 hearing: auditory brainstem responses were impaired upon NgR2 deletion. We discovered
74 both pre- and postsynaptic alterations of IHC-SGN synapses in NgR2$^{-/-}$ mice: presynaptic Ca^{2+}
75 channels of IHCs required stronger depolarization to activate and PSDs seemed deficient of
76 GluA2/3. Additionally, a subset of type I SGN neurites did not contact IHCs but likely still
77 feature "orphan" PSDs.

78

79 # Results

80 ## NgR2 is expressed both in hair cells and spiral ganglion neurons

81

82 Recent transcriptomic data had detected NgR2 expression both in hair cells and SGNs (Elkon
83 et al., 2015; Liu et al., 2018; Shrestha et al., 2018; Jean et al., 2023). We verified this by
84 performing RNAscope staining in mid-modiolar sections of the cochlea and detected
85 expression of NgR2 mRNA both in outer and inner hair cells, as well as SGNs (Figure 1B, C).
86 Spiral ganglia of NgR2$^{-/-}$ mice were lacking NgR2-specific mRNA puncta (Figure 1C),
87 demonstrating specific detection of NgR2 expression in hair cells and SGNs. Next, we
88 performed immunostaining and found specific NgR2 immunofluorescence in SGN somata,
89 which was not present in the absence of the primary antibody (Figure 1D, E) or on SGN somata
90 of NgR2$^{-/-}$ mice (data not shown).

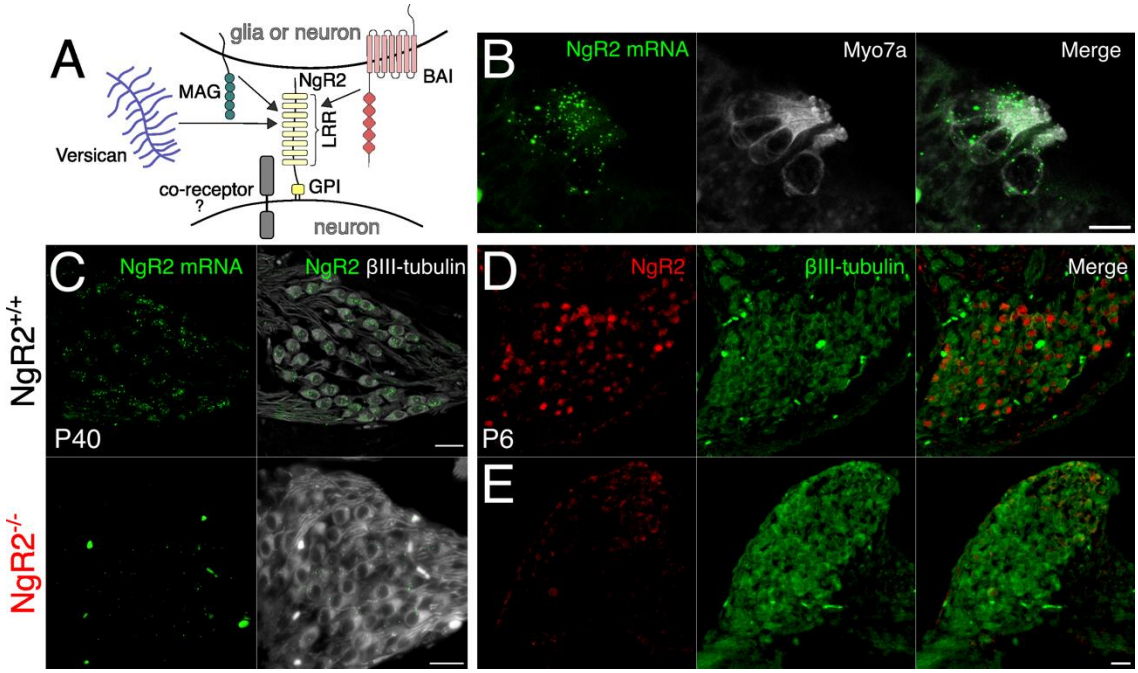

Figure 1. NgR2 mRNA and protein expression in IHCs and SGNs of the mouse cochlea. (**A**) NgR2 is an LRR protein and is anchored to the cell membrane via GPI. In the nervous system NgR2 has been implicated to interact with MAG, versican, BAI. (**B**) Representative images of RNAscope ISH for NgR2 mRNA (green dots) in the hair cell region of p1 wild-type animals. Hair cells are visualized with anti-Myo7a stainings. Scale bar = 10 μm. (**C**) Representative images of RNAscope ISH for NgR2 mRNA (green dots) combined with immunostaining for neuron-specific marker βIII-tubulin (grey) in paraffin sections of p40 NgR2$^{+/+}$ and NgR2$^{-/-}$ spiral ganglion sections. Scale bar = 20 μm. (D) Double immunostaining with anti-NgR2 and βIII-tubulin on cryosections of p6 spiral ganglia. Immunoreactivity of NgR2 (red) was colocalized with βIII-tubulin positive neurons (grey). (E) No specific signal was detected by omitting the primary NgR2 antibody (negative control). Scale bar = 20 μm.

NgR2 is important for the correct development of the auditory afferent synapses

To probe the role of NgR2 in the cochlea, we first studied the numbers of cochlear cells in NgR2$^{-/-}$ mice. We did not observe any change in SGN density or counts of inner and outer hair cells at p15, 1-month- and 2-month-old mice (Figure 2-figure supplement 1). Given that NgR2 has been implicated in synapse formation and development (Wills et al., 2012; Borrie et al., 2014; Wang et al., 2021) we immunolabeled IHC afferent synapses for presynaptic RIBEYE/Ctbp2 and postsynaptic Homer1 in mice at the age of 3 weeks. While we did not detect any change in the number of synaptic ribbons in NgR2$^{-/-}$ IHCs, ribbon volumes were bigger (Figure 2C, D; Figure 2-figure supplement 2). Interestingly, in addition to the Homer1 positive puncta juxtaposing presynaptic ribbons, we observed additional Homer1 patches, which

115 appeared to be away from IHCs, potentially marking “orphan” PSDs (Figure 2A, B). Moreover,
116 the Homer1 puncta juxtaposing IHC AZs were significantly smaller in NgR2$^{-/-}$ mice compared
117 to the control IHCs (Figure 2E). While we found the percentage of presynaptic ribbons
118 juxtaposing Homer1 immunofluorescent puncta to be decreased by approximately 7% in
119 NgR2$^{-/-}$ mice (Figure 2F), we cannot exclude that our immunolabeling protocol lacked the
120 sensitivity to detect smaller synaptically engaged PSDs. Out of the four pore-forming AMPA
121 receptor subunits (GluA1-4), mature SGNs express GluA2-4 (Niedzielski and Wenthold, 1995;
122 Matsubara et al., 1996). Our immunolabeling of anti-GluA2/3 revealed a severe reduction of
123 GluA2/3 positive puncta in NgR2$^{-/-}$, indicating possible lack or decrease of GluA2/3 (Figure 2-
124 figure supplement 3A, B). Interestingly, the remaining GluA2/3 patches did not properly
125 juxtapose presynaptic ribbons (Figure 2-figure supplement 3C). Despite this, the expression of
126 Gria2 RNA appeared to be maintained in SGNs, as indicated by RNAscope (Figure 2-figure
127 supplement 3D). To check if the “orphan” PSDs away from IHCs were possibly erroneously
128 engaged with efferent presynaptic terminals we stained the latter for synapsin, which is
129 lacking from IHCs, but did not observe any obvious juxtaposition between the “orphan”
130 Homer1 and synapsin puncta (Figure 2-figure supplement 4).

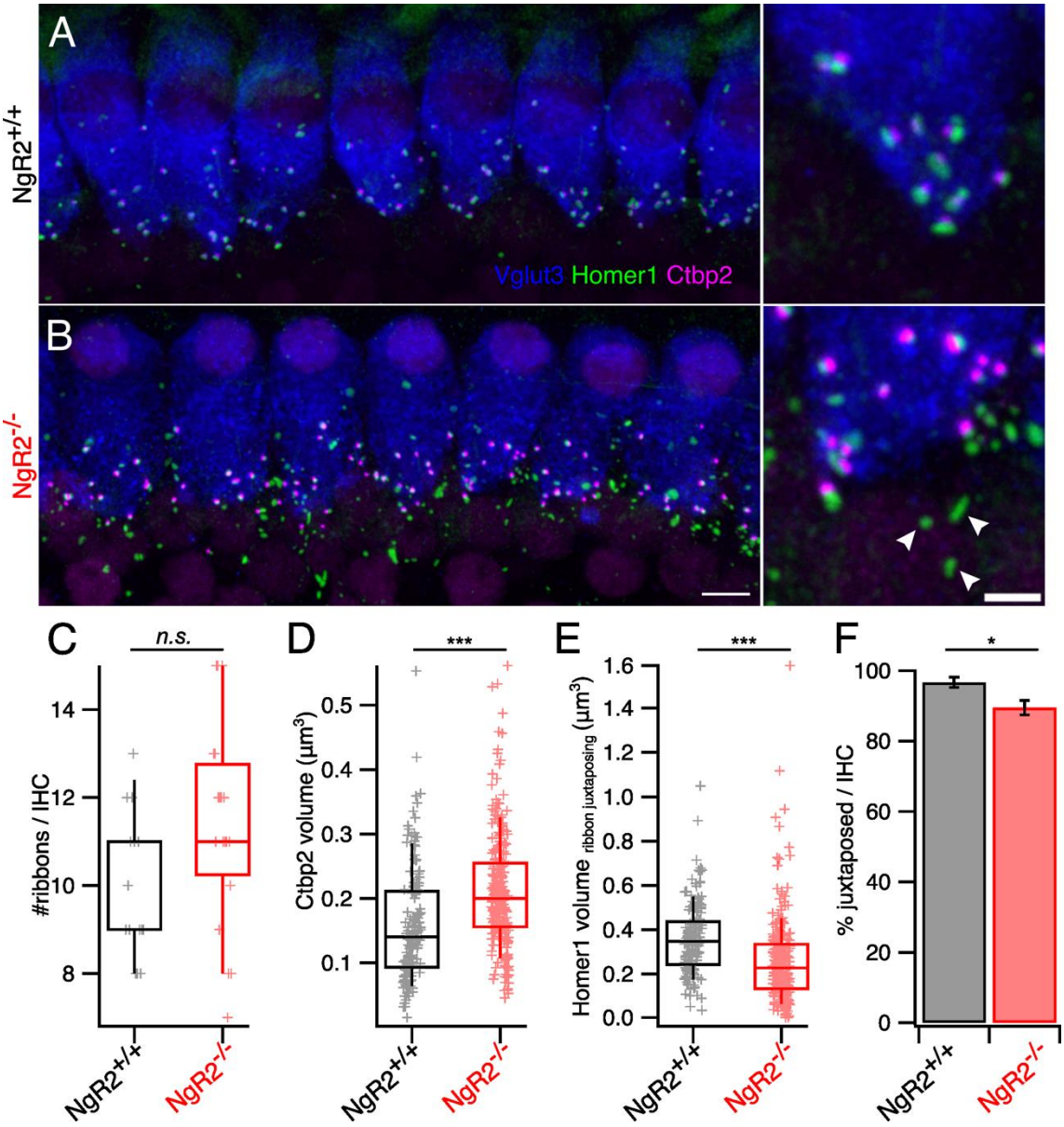

Figure 2. Pre- and postsynaptic changes at IHCs of NgR2$^{-/-}$ mice. (**A, B**) Maximal intensity projections of representative confocal stacks of IHCs from NgR2$^{+/+}$ (A) and NgR2$^{-/-}$ (B) mice immunolabeled against Vglut3, Homer1, and Ctbp2. Scale bar = 5 µm. Images on the right-hand side are zoomed into the synaptic regions. Scale bar = 2 µm. Some of the putative "orphan" PSDs are marked with the white arrowheads. (**C**) Number of Ctbp2 positive puncta is not changed in IHCs of NgR2$^{-/-}$ mice (NgR2$^{+/+}$: 9.9 ± 0.42, SD = 1.62, n = 15, N = 2 vs NgR2$^{-/-}$: 11.4 ± 0.5, SD = 2.25, n = 20, N = 3; p = 0.06, Mann-Whitney-Wilcoxon test). (**D**) Ribbon volumes are enlarged in NgR2$^{-/-}$ IHCs (NgR2$^{+/+}$: 0.16 ± 0.007 µm^3, SD = 0.09 µm^3, n = 165, N = 2 vs NgR2$^{-/-}$: 0.21 ± 0.005 µm^3, SD = 0.09 µm^3, n = 259, N = 3; p < 0.001, Mann-Whitney-Wilcoxon test). (**E**) Homer1 patches which are juxtaposing presynaptic ribbons show decreased volumes in NgR2$^{-/-}$ IHCs (NgR2$^{+/+}$: 0.36 ± 0.01 µm^3, SD = 0.16 µm^3, n = 160, N = 2 vs NgR2$^{-/-}$: 0.26 ± 0.01 µm^3, SD = 0.19 µm^3, n = 249, N = 3; p < 0.001, Mann-Whitney-Wilcoxon test). (**F**) Percentage of Ctbp2 puncta juxtaposing Homer1 is slightly decreased in NgR2$^{-/-}$ mice (NgR2$^{+/+}$: 96.7 ± 1.45 %, SD = 5.44 %, n = 14, N = 2 vs NgR2$^{-/-}$: 89.5 ± 2.05 %, SD = 9.18 %, n =

20, N = 3; p = 0.03, Mann-Whitney-Wilcoxon test). Data is presented as mean ± SEM. Box-whisker plots show the median, 25/75 percentiles (box), and 10/90 percentiles (whiskers). Individual data points are overlaid.

Additional non-synaptic neurites in the cochlea of NgR2$^{-/-}$ mice

To further examine the afferent cochlear connectivity, we utilized serial block-face scanning electron microscopy (SBEM) to 3D reconstruct the apical cochlea segments from two NgR2$^{-/-}$ and one littermate NgR2$^{+/+}$ control mice at p36 (Figure 3A). As recently demonstrated (Hua et al., 2021; Lu et al., 2024), the spatial resolution of SBEM allows reliable ribbon synapse identification and neurite reconstruction (Figure 3B and C). In these three datasets, we have traced 133 neural fibers from their postsynaptic ending in the organ Corti towards the modiolus, of which 115 were classified as peripheral neurites of type I SGN based on their radial calibers and extensive myelination after entering the habenula perforata (Figure 3D). We observed a substantial number of neurites that did not engage the IHCs (non-synaptic neurites) in the NgR2$^{-/-}$ organs of Corti (23 out of 83) in contrast to the wild-type control (3 out of 32, Figure 3E). Although most non-synaptic neurites were found in the inner spiral bundle, they failed to reach IHC basal lateral poles to form contacts (17 out of 23 in NgR2$^{-/-}$ animals). This result might provide a plausible explanation for the “orphan” Homer1 puncta shown by immunohistochemistry in NgR2$^{-/-}$ organs of Corti. Note that the presence of non-synaptic neurites in the NgR2$^{-/-}$ animal was not associated with a profound reduction in ribbon synapses (Figure 2C, Figure 2-figure supplement 2B, Figure 3-figure supplement 1A), suggesting a different scenario than deafferentation due to excitotoxic synaptopathy as recently reported (Moverman et al., 2023). Nevertheless, nearly all traced radial fibers were found predominantly unbranched in both the NgR2$^{-/-}$ (97%) and the wild-type control mice (94%; Figure 3F).

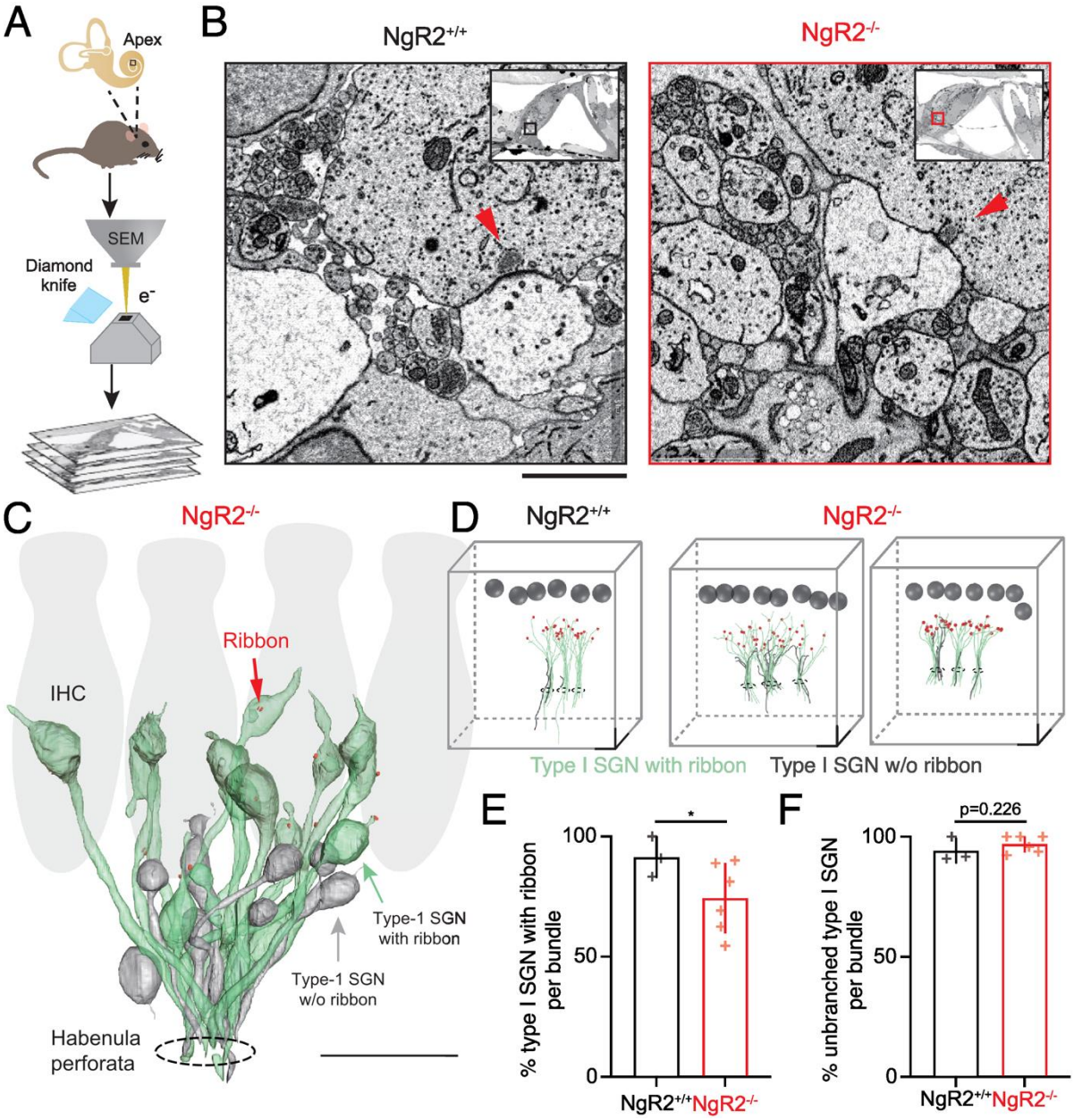

Figure 3. Additional non-synaptically engaged SGN neurites in the cochlea of NgR2$^{-/-}$ mice. (**A**) Workflow of SBEM imaging at the mouse apical cochlear region. (**B**) Example images of neurites beneath IHCs from the NgR2$^{+/+}$ (left) and NgR2$^{-/-}$ (right) mice. Synaptic ribbons are indicated with red arrows. The regions of interest were magnified from single sections of SBEM datasets (insets). Scale bar = 2 µm. (**C**) 3D rendering of afferent fiber reconstruction with ribbons (red), showing both synaptic (green, type I SGN with ribbon) and non-synaptic (grey, type I SGN without ribbon) populations in the NgR2$^{-/-}$ mouse. Scale bar = 10 µm. (**D**) Display of classified radial fibers in the NgR2$^{+/+}$ (left) and NgR2$^{-/-}$ (middle and left) animals. All fibers were traced from the habenula perforata (cycles) before classification to avoid bias to terminal types. Scale bar 10 µm. (**E**) Percentage of radial fibers with ribbon per bundle (NgR2$^{+/+}$: 91.41 ± 8.35 %, n = 3 bundles, N = 1 vs NgR2$^{-/-}$: 74.40 ± 14.58%, n = 6 bundles, N = 2; p = 0.032, unpaired t-test). (**F**) Percentage of unbranched radial fibers per bundle (NgR2$^{+/+}$:

185 94.19 ± 5.04 %, n = 3 bundles, N = 1 vs NgR2$^{-/-}$: 96.98 ± 3.49 %, n = 6 bundles, N = 2; p = 0.226,
186 unpaired t-test).

187 ## Deletion of NgR2 results in depolarized shift of the Ca^{2+} channel activation in IHCs
188

189 Next, we tested for potential effects of NgR2 deletion on the presynaptic IHC function. We
190 performed whole-cell patch-clamp recordings from IHCs of p21-29 NgR2$^{-/-}$ and NgR2$^{+/+}$ mice.
191 First, we recorded voltage-gated Ca^{2+} currents by applying step depolarizations with 5 mV
192 increment in ruptured patch-clamp configuration (Figure 4A, see Materials and Methods). We
193 did not observe any change in the maximal Ca^{2+} current amplitude (Figure 4B, C), yet noticed
194 small (~ +3 mV) but consistent and statistically significant depolarized shift of the voltage of
195 half-maximal Ca^{2+} channel activation (V_{half}; Figure 4D, E). The voltage sensitivity of the
196 channels was not changed in NgR2$^{-/-}$ IHCs (Figure 4F). Next, we probed Ca^{2+} influx triggered
197 exocytosis from IHCs by applying depolarizations of varying durations to voltages saturating
198 Ca^{2+} influx in IHCs of both genotypes (-17 mV) and recording exocytic membrane capacitance
199 changes (ΔC_m) in the perforated patch-clamp configuration (Figure 4G). Both fast (up to 20 ms
200 depolarization) and sustained components of exocytosis remained intact in the mutant,
201 indicating unaffected readily releasable pool and replenishment of the vesicles in NgR2$^{-/-}$ IHCs
202 (Figure 4H).

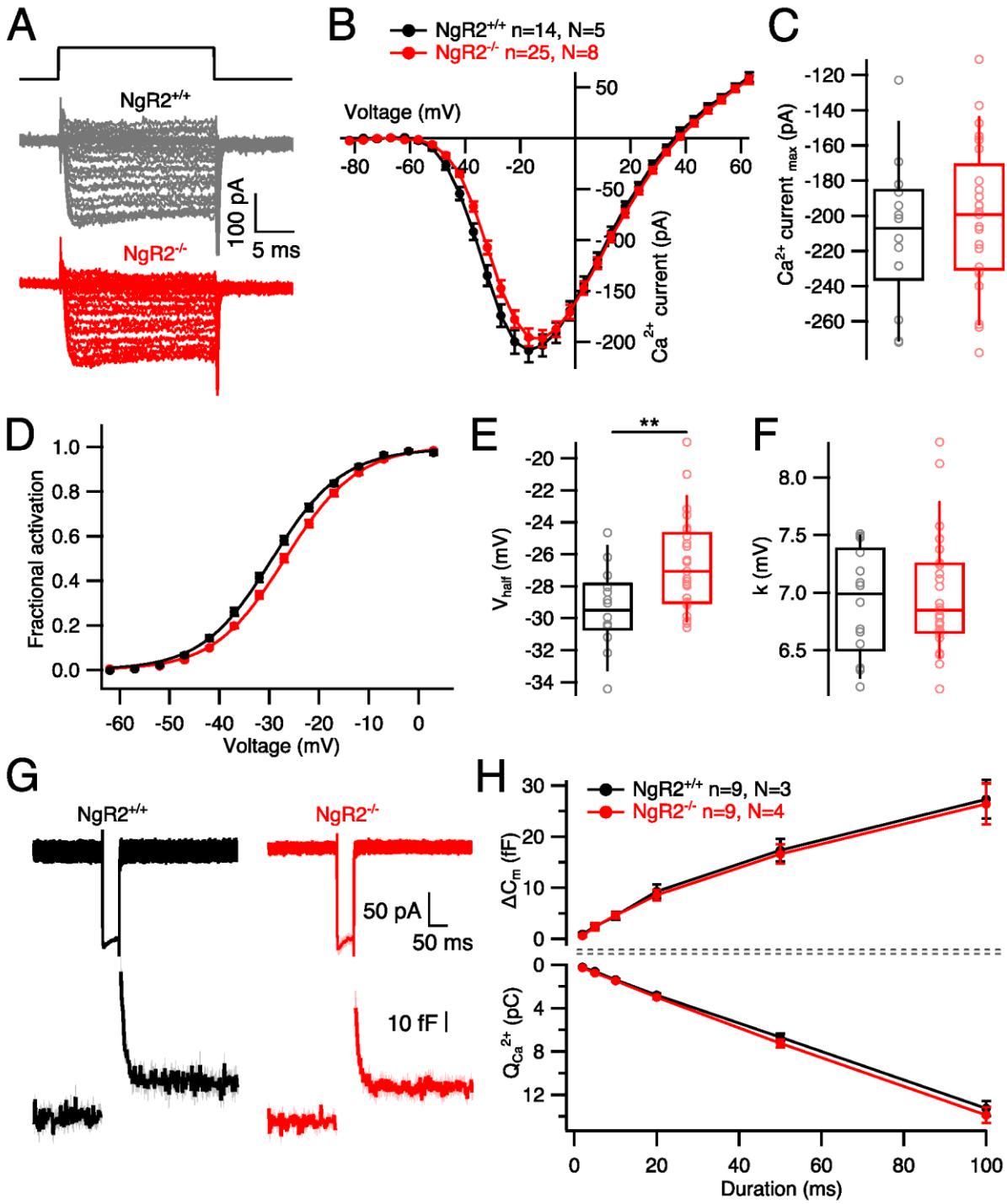

Figure 4. Shifted operation range of Ca^{2+} channels but intact exocytosis in IHCs of $NgR2^{-/-}$ mice. (**A**) Representative current traces from IHCs of $NgR2^{+/+}$ (top, black) and $NgR2^{+/+}$ (bottom, red) evoked by step depolarizations. (**B**) Average Ca^{2+} current-voltage relationships (IV curves) in $NgR2^{+/+}$ and $NgR2^{-/-}$ IHCs. (**C**) Maximal Ca^{2+} current amplitude is not changed in $NgR2^{-/-}$ IHCs ($NgR2^{+/+}$: 210 ± 10.9 pA, SD = 40.9 pA, n = 14, N = 5 vs $NgR2^{-/-}$: -200 ± 8.19 pA, SD = 40.9 pA, n = 25, N = 8; p = 0.47, Student's t-test). (**D**) Fractional activation curves of Ca^{2+} channels calculated from IVs show depolarized shift in channel activation in $NgR2^{-/-}$ IHCs. (**E**) Voltage of half maximal activation obtained from Boltzmann fit of the curves from (D) is more positive in

212 NgR2$^{-/-}$ IHCs (NgR2$^{+/+}$: -29.4 ± 0.66 mV, SD = 2.48 mV, n = 14, N = 5 vs NgR2$^{-/-}$: -26.6 ± 0.59 mV,
213 SD = 2.94 mV, n = 25, N = 8; p = 0.004, Student's t-test). (**F**) Voltage sensitivity (k) is not changed
214 in NgR2$^{-/-}$ IHCs (NgR2$^{+/+}$: 6.92 ± 0.12 mV, SD = 0.46 mV, n = 14, N = 5 vs NgR2$^{-/-}$: 6.98 ± 0.1 mV,
215 SD = 0.51 mV, n = 25, N = 8; p = 0.93, Mann-Whitney-Wilcoxon test). (**G**) Average current traces
216 evoked by 50 ms depolarization to -17mV (top row) and resulting capacitance response
217 (bottom row) from NgR2$^{+/+}$ (left, black) and NgR2$^{+/+}$ (right, red) IHCs. Shaded areas represent
218 ± SEM. (**H**) Exocytic capacitance change (ΔC_m, top) and corresponding Ca^{2+} charge ($Q_{Ca}{}^{2+}$,
219 bottom) evoked by depolarizations (to -17 mV) of various durations (2, 5, 10, 20, 50, 100 ms).
220 Box-whisker plots show the median, 25/75 percentiles (box) and 10/90 percentiles (whiskers).
221 Individual data points are overlaid.
222
223 We then turned to study single AZ function by combining whole cell ruptured patch-clamp
224 combined with spinning disc confocal imaging of presynaptic Ca^{2+} influx, as described
225 previously (Ohn et al., 2016). TAMRA conjugated Ctbp2 binding dimeric peptide and the low
226 affinity Ca^{2+} indicator Fluo4-FF (k_D: 10 µM) were loaded into the cell via the patch pipette and
227 Ca^{2+} influx at single AZs was visualized in the form of hotspots by applying voltage ramp
228 depolarizations to the IHCs and simultaneously imaging Fluo4-FF fluorescence near labeled
229 ribbons (Figure 5A, see Materials and methods). Maximal Ca^{2+} influx at single AZs tended to
230 be higher in IHCs of NgR2$^{-/-}$ mice but the difference did not reach statistical significance (Figure
231 5B, B^{i}). The V_{half} of Ca^{2+} channel clusters at single AZs showed depolarized shift (~ +5 mV),
232 which was statistically significant despite the large variability of V_{half} across different AZs
233 (Figure 5C, C^{i}). Furthermore, we did not observe any mismatch in Ctbp2 positive puncta and
234 evoked Ca^{2+} hotspots, indicating the correct localization of Ca^{2+} channels at the AZs. We
235 verified this by performing immunostainings of $Ca_v1.3$, Ctbp2 and Bassoon and did not detect
236 any apparent misalignment of these protein clusters (Figure 5D). In summary, deletion of
237 NgR2 causes a depolarized shift of the activation of presynaptic Ca^{2+} influx in IHCs as
238 demonstrated at the single AZ and whole cell levels. This is expected to elevate the sound
239 pressure levels required to reach a comparable activity of synaptic transmission for sound
240 encoding and predicts elevated auditory thresholds which we tested by recordings of auditory
241 brainstem responses.

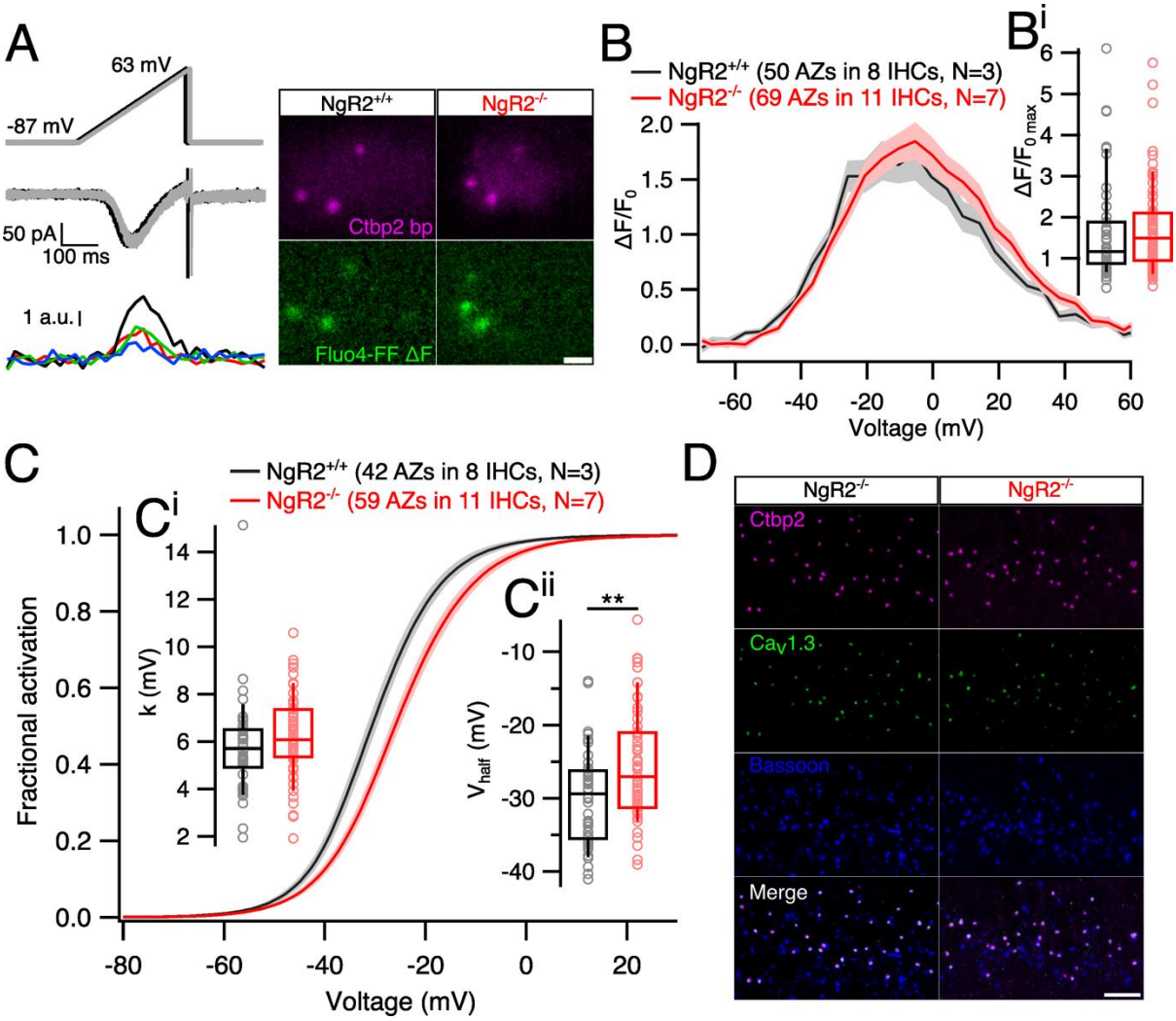

Figure 5. Depolarized shift of Ca^{2+} channel activation at single AZs but intact presynaptic organization in $NgR2^{-/-}$ IHCs. (**A**) Voltage ramp stimulation protocols (top), evoked whole cell currents (middle) and the presynaptic hotspots of Fluo4-FF fluorescence (bottom) of a representative IHC recording. Black and grey colors represent the two stimulations, one being 5 ms shifted over the other. Images on the right show single image planes of representative $NgR2^{+/+}$ (left) and $NgR2^{-/-}$ (right) IHCs filled with TAMRA conjugated Ctbp2 binding peptide (Ctbp2 bp) and Fluo4-FF Ca^{2+} dye. Ca^{2+} hotspots are visualized by subtracting the average of baseline planes from the average of 5 planes during stimulation. Scale bar = 2 µm (**B**) Average fluorescence-voltage relationships of Ca^{2+} influx at single AZ from $NgR^{+/+}$ and $NgR2^{-/-}$ IHCs show no difference in the maximal Ca^{2+} amplitude (**B^{i}**; $NgR2^{+/+}$: 1.6 ± 0.17, SD = 1.2, n = 50 AZs vs $NgR2^{-/-}$: 1.7 ± 0.13 pA, SD = 1.09, n = 69 AZs; p = 0.24, Mann-Whitney-Wilcoxon test). Shaded areas represent ± SEM. (**C**) Average fractional activation curves of Ca^{2+} channels at single AZs relationships of single AZ show intact voltage sensitivity (**C^{i}**; $NgR2^{+/+}$: 5.79 ± 0.32 mV, SD = 2.04 mV, n = 42 AZs vs $NgR2^{-/-}$: 6.25 ± 0.22 mV, SD = 1.7 mV, n = 59 AZs; p = 0.06, Mann-Whitney-Wilcoxon test) but depolarized shift of V_{half} (**C^{ii}**; $NgR2^{+/+}$: -30 ± 1 mV, SD = 6.5 mV, n = 42 AZs vs $NgR2^{-/-}$: -25.5 ± 0.98 mV, SD = 7.49 mV, n = 59 AZs; p = 0.002, Student's t-test) in $NgR2^{-/-}$ IHCs. Shaded areas represent ± SEM. (**D**) Representative immunolabelings of presynaptic proteins show no apparent mislocalization in $NgR2^{-/-}$ IHCs. Scale bar = 5 µm. Box-whisker plots show the median, 25/75 percentiles (box) and 10/90 percentiles (whiskers). Individual data points are overlaid.

NgR2 is essential for normal hearing

In order to evaluate auditory systems function in NgR2$^{-/-}$ mice, we recorded auditory brainstem responses (ABRs) at the age of 2-4 months. ABRs were elicited in response to 4, 8, 16, 32 kHz tone bursts and click stimuli of increasing sound pressure levels. We determined the sound thresholds by identifying the lowest sound pressure level which resulted in detectable ABR waveform. We found ABR thresholds to be significantly increased by around 30-45 dB across all the tested frequencies and in response to the click stimulations in NgR2$^{-/-}$ mice compared to the wild-type controls (Figure 6). NgR2$^{+/-}$ mice showed an intermediate phenotype between the NgR2$^{-/-}$ and NgR2$^{+/+}$ mice with a lower yet significant increase of ABR thresholds of approximately 10-15 dB at 4, 16 and 32 kHz frequencies.

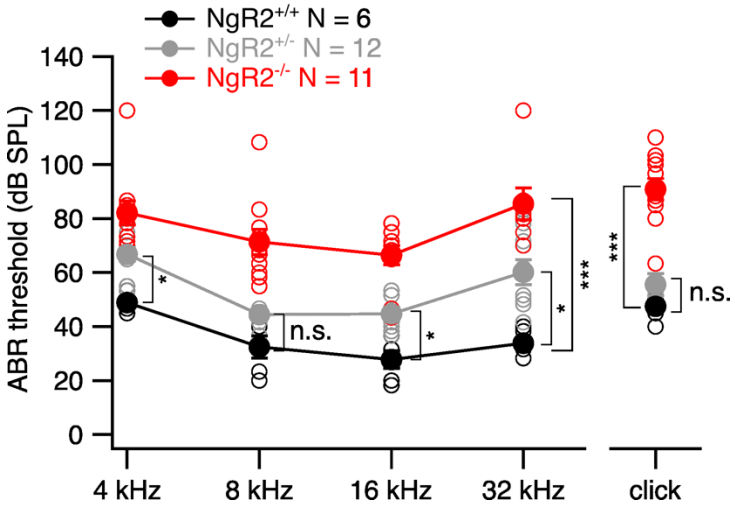

Figure 6. Elevated acoustic thresholds in NgR2$^{-/-}$ mice. ABR thresholds were measured in response to 4, 8, 16, 32 kHz tone bursts and click stimuli. ABR thresholds of individual animals are shown in open circles on top of the mean ± SEM. Statistical significances are reported as *p < 0.05, ***p < 0.001, Kruskal-Wallis followed by Dunn's multiple comparison test.

Discussion

In this study, we investigated the role of the Nogo-66 receptor homolog NgR2 in the cochlea. Consistent with the previous reports, we detected NgR2 expression in IHCs and SGNs. Upon NgR2 deletion, we observed alterations of the IHC-SGN synapses (Figure 7). Presynaptically, Ca^{2+} channel activation was shifted towards depolarized voltages and ribbon size was enlarged. IHC exocytosis was unaltered when probed at saturating depolarizations. At the postsynaptic side, PSDs juxtaposing presynaptic ribbons were smaller compared to the controls and seemed to be deficient of GluA2/3, despite the expression of Gria2 mRNA in

289 NgR2$^{-/-}$ SGNs. Additionally, we observed PSDs which resided further from the IHC membrane
290 and did not juxtapose the presynaptic AZs in NgR2$^{-/-}$ mice. These PSDs potentially belong to
291 the type I SGN neurites that ended in the inner spiral bundle without contacting the IHCs, as
292 observed in SBEM reconstructions of NgR2$^{-/-}$ SGNs. Finally, ABR thresholds were elevated in
293 NgR2$^{-/-}$ mice indicating that NgR2 is required for normal hearing.
294

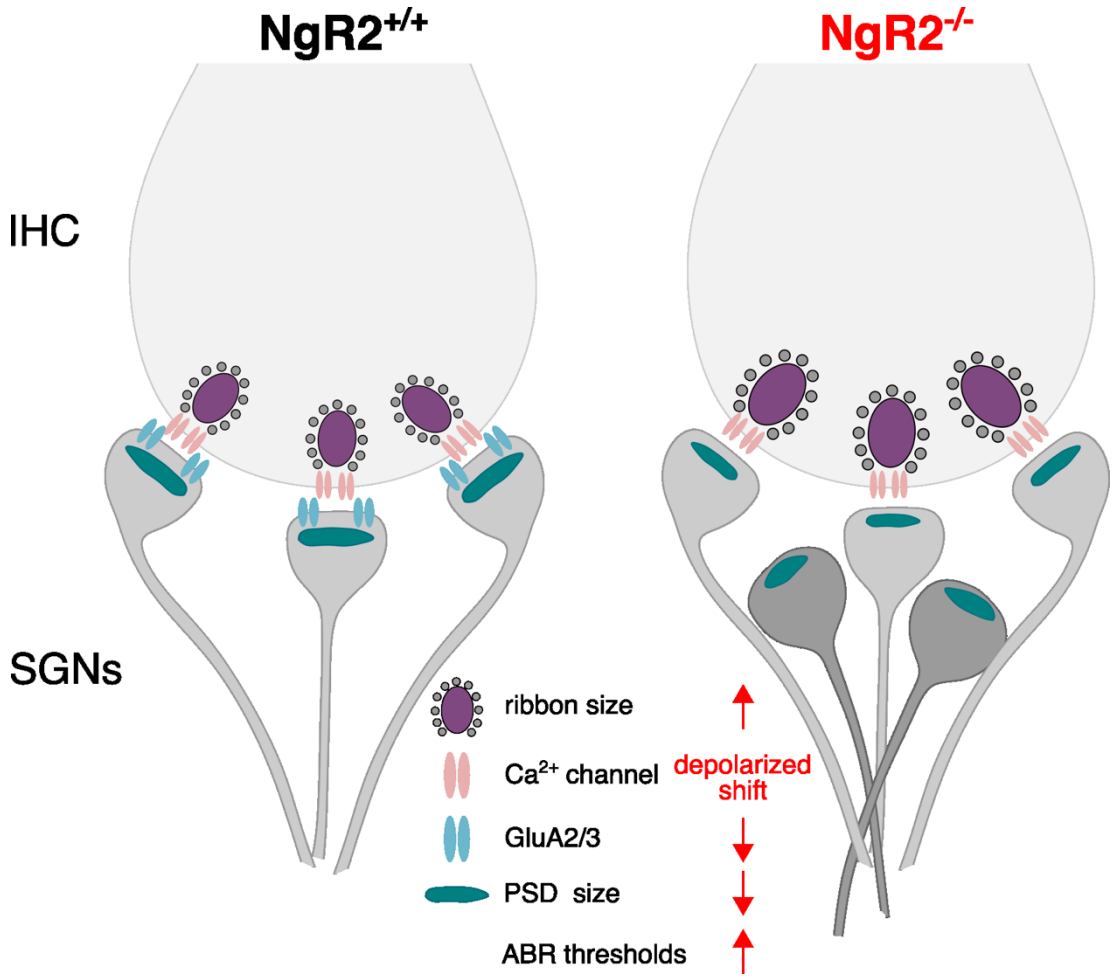

295

296 **Figure 7. Schematic illustration of the key structural and functional changes in the auditory**
297 **periphery of NgR2$^{-/-}$ mice.** NgR2$^{-/-}$ mice display enlarged synaptic ribbons and depolarized
298 shift in the activation of presynaptic Ca^{2+} channels in IHCs, as well as reduced size of PSDs
299 juxtaposing presynaptic ribbons. NgR2 deficiency further results in a subset of type I SGN
300 neurites that reach the inner spiral bundle but do not engage the IHCs.
301
302 The changes of presynaptic Ca^{2+} channel properties and ribbons in IHCs could result
303 from either i) a presynaptic action of NgR2 or ii) from NgR2 acting in the postsynaptic SGNs,
304 with an impact on transsynaptic signaling to IHCs. Presynaptic changes upon postsynaptic
305 manipulation have been reported previously. For instance, the deletion of postsynaptically
306 expressed Pou4f1 transcription factor resulted in hyperpolarized shift of IHC Ca^{2+} channels, as

307 well as in changes of the presynaptic heterogeneity of IHC AZs (Sherrill et al., 2019). Similarly,
308 presynaptic ribbon sizes were altered in IHCs of mice, which exhibited conditional deletion of
309 Runx1 transcription factor from SGNs (Shrestha et al., 2023).

310 We did not detect NgR2 near the synaptic regions but cannot exclude transient
311 synaptic localization of NgR2 during development. Indeed, NgR localization has been shown
312 to be dynamically regulated across different phases of IPSC-derived neuron development
313 (Wang et al., 2021). We propose that the afferent synaptic changes contribute to the severe
314 hearing impairment in NgR2$^{-/-}$ mice. The phenotype of increased ABR thresholds could
315 partially be explained by the depolarized activation of Ca^{2+} channels in IHCs. As it has been
316 shown, the apparent Ca^{2+} dependence of glutamate release from IHCs on average follows a
317 near linear relationship (Wong et al., 2014; Özçete and Moser, 2021; Jaime Tobón and Moser,
318 2023b, 2023a). Therefore, due to the depolarized shift of the Ca^{2+} channel activation, the
319 glutamate release from IHCs and subsequent spike generation in SGNs would require stronger
320 stimuli. Likewise, depolarized activation of Ca^{2+} channels has been associated with the higher
321 firing thresholds and low spontaneous rates in SGNs of Ribeye knock-out mice, albeit less
322 severe hearing phenotype was observed in those mice (Jean et al., 2018).

323 In addition or alternatively, the increase in auditory thresholds could be caused by the
324 deficiency of GluA2/3 AMPA receptors of the SGN postsynapses in NgR2$^{-/-}$ mice. We cannot
325 exclude that the lack of GluA2/3 subunits can be compensated by the overexpression of GluA4
326 subunit, which was also recently shown in GluA3 KO mice (Rutherford et al., 2023). Given the
327 observed synaptic changes, it seems less likely that the hearing impairment would have
328 resulted from the intrinsic changes of SGN firing. Further experiments, where SGNs would be
329 stimulated directly via *ex vivo* patch-clamp or optogenetically could help to probe for
330 functional deficits in SGN of NGR2$^{-/-}$ mice. Another interesting observation was the additional
331 PSDs not juxtaposing presynaptic ribbons that were detected around IHCs of NgR2$^{-/-}$ mice.
332 These "orphan" PSDs seem not to be part of the efferent synapses formed between
333 LOC/MOCs and SGNs as we verified by simultaneous anti-Homer1 and anti-synapsin
334 immunolabelings. To check the SGN connectivity we performed SBEM in NgR2$^{+/+}$ and NgR2$^{-/-}$
335 cochlear samples and observed a high percentage of non-synaptic SGN neurites in the
336 reconstructed neurons of inner spiral bundles in NgR2$^{-/-}$ samples. A sizable subset of the non-
337 synaptic SGN boutons did not make a contact with IHCs, potentially housing the "orphan"
338 PSDs observed around the IHCs in our immunolabeled samples. How exactly those non-

339 synaptic neurites appear remains to be investigated. SGN neurite retraction from IHCs has
340 been demonstrated in noise-exposed animals, followed by the degeneration of the SGN
341 somata and axons (Kujawa and Liberman, 2009, 2015; Moverman et al., 2023). This process
342 however results in up to 50% degeneration of the ribbon synapses. Interestingly, in NgR2$^{-/-}$
343 mice the number of the ribbon synapses as well as the density of the SGN somata was largely
344 intact. This indicates that the non-synaptic neurites do not result from synaptic loss as found
345 in hereditary or acquired synaptopathy (Roux et al., 2006; Ruel et al., 2008; Seal et al., 2008;
346 Kujawa and Liberman, 2009). Although it is plausible that the non-synaptic SGN neurites may
347 fail to reach the IHCs during initial development, it is unlikely that this would selectively impact
348 only a subset of neurons and still allow the Homer1-positive patches to develop in the absence
349 of presynaptic components. Alternatively, it is known that major synaptic pruning takes place
350 in developing SGNs, whereby up to 50% of the synapses are lost between the IHCs and the
351 SGNs (Defourny et al., 2013; Coate et al., 2019), suggesting, that the non-synaptic SGN
352 neurites of NgR2$^{-/-}$ mice could be a result of failed pruning of SGNs during the development.
353 Yet how this would then comply with normal synapse and SGN counts remains to be
354 elucidated. Future studies will be required to quantify the type I SGN projections of NgR2$^{-/-}$
355 mice during development and to trace their neurites from the soma to the organ of Corti to
356 probe for potential branching in the spiral lamina.

357 Future work will be required to identify the NgR2 ligands in the cochlea. To this date,
358 NgR interaction partners are not very well understood. While NgR1 in-trans interactions
359 include NogoA, MAG, OMgp, chondroitin sulfate proteoglycans, the only well established
360 ligand for NgR2 remains MAG (Fournier et al., 2001; Domeniconi et al., 2002; Wang et al.,
361 2002; Venkatesh et al., 2005; Schwab, 2010). Other attractive candidate ligands for NgRs are
362 the brain-specific angiotensin inhibitor (BAI) adhesion GPCRs. BAI-NgR interaction has been
363 suggested to mediate dendritic arborization, axonal elongation, and synapse formation in
364 IPSCs (Wang et al., 2021). Interestingly, a recent study described a hearing impairment in BAI1
365 deficient mice and suggests that BAI1 is important for correct localization of AMPA receptor
366 subunits in spiral ganglion neurons based on the absence or decrease of different AMPA
367 receptor subunits at the SGN postsynapses in BAI1 deficient mice (Carlton et al., 2024).
368 Similarly, our data from NgR2$^{-/-}$ mice show the absense of GluA2/3 positive puncta juxtaposing
369 presynaptic AZs. While BAI1 is suggested to act exclusively in SGNs (Carlton et al., 2024), NgR2
370 is expressed in both IHCs and SGNs. Along with the evidence for transsynaptic interaction

371 between NgRs and BAIs (Wang et al., 2021), this raises the possibility that the GluA2/3 AMPA
372 receptor subunit localization to SGN PSDs requires the interaction of presynaptic NgR2 and
373 postsynaptic BAI1. Alternatively, NgR2 expression in SGNs might be directly involved in
374 GluA2/3 tethering.

375 Finally, NgR2 has been proposed to interact with chondroitin-sulfate proteoglycan
376 Versican to control the amount of skin innervation by DRG neurites (Bäumer et al., 2014).
377 While to our knowledge, attempts have yet to be made for detecting Versican signal around
378 the IHCs, other extracellular matrix proteins such as aggrecan, brevican, Tenascin-R, Tenascin-
379 C, hyaluron and proteoglycan link proteins 1 and 4 have been shown to form dense, basket-
380 like structures that surround the base of the IHCs (Kwiatkowska et al., 2016; Sonntag et al.,
381 2018). Furthermore, deletion of brevican results in alteration of pre- and postsynaptic spatial
382 coupling at IHC synapses, indicating the possible role of extracellular matrix in transsynaptic
383 organization. However, while the existing observations suggest that the synaptic changes in
384 NgR2 deficient animals might reflect derailed interaction of the SGN neurites with the
385 extracellular matrix, the relevance of such an interaction of NgR2 and Versican in the cochlea
386 needs to be addressed in the future.

387

Materials and Methods

Animals

NgR2 null mutant mice on a C57BL/6N background were generated as previously described (Wörter et al., 2009). Knock-out ($NgR2^{-/-}$) and wild-type ($NgR2^{+/+}$) mice were derived from heterozygous matings. Both male and female mice were used in this study. Animals were genotyped as previously described (Wörter et al., 2009). The ages of the mice varied depending on the experiment as noted in the manuscript. The breeding and the experiments were approved by the Institutional Animal Care and Use Committee at the Medical University of Innsbruck, local Animal Welfare Committee of the University Medical Center Göttingen and the Max Planck Institute for Multidisciplinary Sciences, as well as the Animal Welfare Office of the state of Lower Saxony, Germany (LAVES, AZ: 19/3134). The ABR experiments were carried out under the approval of the Austrian Ministry of Education, Science and Research (reference number BMWFW-66.011/0120-WF/V/3b/2016).

Patch-clamp recordings

The apical turn of the organ of Corti was dissected from p21 to p29 animals in HEPES Hanks solution containing (in mM): 5.36 KCl, 141.7 NaCl, 10 HEPES, 0.5 $MgSO_4$, 1 $MgCl_2$, 5.6 D-glucose, and 3.4 L-glutamine (pH 7.2, ~ 300 mOsm/l). IHCs were exposed by gently removing of nearby supporting cells by negative pressure through a glass pipette from either modiolar or pillar side. All experiments were conducted at room temperature (RT, 20–25°C). Patch pipettes were made from GB150-8P or GB150F-8P borosilicate glass capillaries (Science Products, Hofheim, Germany) for perforated and ruptured patch-clamp configurations, respectively. Pipettes were fire polished with a custom-made microforge and coated with Sylgard to minimize the capacitive noise, whenever capacitance recordings were performed. The measurements were performed using EPC-10 amplifier controlled by Patchmaster software (HEKA Elektronik, Germany). The holding potential for IHCs was set to -87 mV across all the experiments.

Ruptured patch-clamp

421 For ruptured patch-clamp we used extracellular solution containing (in mM): 2.8 KCl, 105 NaCl,
422 10 HEPES, 1 CsCl, 1 $MgCl_2$, 5 $CaCl_2$, 35 TEA-Cl, and 2 mg/ml D-glucose (pH 7.2, ~ 300 mOsm/l).
423 Intracellular solution contained in mM: 111 Cs-glutamate, 1 $MgCl_2$, 1 $CaCl_2$, 10 EGTA, 13 TEA-
424 Cl, 20 HEPES, 4 Mg-ATP, 0.3 Na-GTP and 1 L-glutathione (pH 7.3, ~ 290 mOsm/l). Additionally,
425 Ca^{2+} indicator Fluo4-FF (0.8 mM, Life Technologies) and TAMRA-conjugated RIBEYE/Ctbp2
426 binding peptide (10 mM, synthetized by the group of Dr. Olaf Jahn, Göttingen) were added to
427 the intracellular solution for live imaging (Zenisek et al., 2004). Voltage dependency of Ca^{2+}
428 influx was recorded by applying 20 ms long step deploarizations with 5 mV increment. For
429 Ca^{2+} imaging, voltage ramp depolarizations ranging from -87 mV to 63 mV in the course of 150
430 ms were applied to the cells. Leak correction was performed using P/n protocol and liquid
431 junction potential of 17 mV was corrected offline. Recordings were discarded from the
432 analysis if the series resistance (R_s) exceeded 14 MOhm during the first 3 minutes after
433 rupturing the cell, leak current exceeded -50 pA at the holding potential and Ca^{2+} current
434 rundown was more than 25%.
435 Recordings were analyzed using Igor Pro 6.3 (Wavemetrics) custom-written programs. Ca^{2+}
436 current-voltage relationships (IV curves) were obtained by averaging approximately 5 ms
437 segments at the maximal activation regions of individual current traces and plotting them
438 against the depolarization voltages. Fractional activation curves of the Ca^{2+} channels were
439 calculated from the IVs and fitted with the Boltzmann function to determine the voltage of
440 half maximal activation (V_{half}) and voltage sensitivity (k).
441

442 ## Perforated patch clamp recordings
443

444 To perform simultaneous membrane capacitance (C_m) and Ca^{2+} current measurements we
445 used extracellular solution containing (in mM): 106 NaCl, 35 TEA-Cl, 2.8 KCl, 1 $MgCl_2$, 1 CsCl,
446 10 HEPES, 3 $CaCl_2$, and 5.6 D-glucose (pH 7.2, ~ 300 mOsm/l). The pipette solution contained
447 (in mM): 137 Cs-gluconate, 15 TEA-Cl, 3 GTP-Na_2, 1 ATP-Mg, 10 HEPES, 1 $MgCl_2$, as well as 300
448 mg/ml amphotericin B (pH 7.17, ~ 290 mOsm/l). Perforated patch-clamp recordings from
449 IHCs was described previously (Moser and Beutner, 2000). C_m changes were measured using
450 Lindau-Neher technique (Lindau and Neher, 1988). To evoke exocytosis IHCs were stimulated
451 by step depolarizations (to -17 mV) of different durations (2, 5, 10, 20, 50, 100 ms) in
452 randomized manner. Currents were leak-corrected using a p/5 protocol. Recordings were used

453 only if the leak current was lower than 30 pA and the R_s was lower than 30 MOhm. Recordings
454 were analyzed using Igor Pro 6.3 (Wavemetrics) custom-written programs. Ca^{2+} charge ($Q_{Ca}{}^{2+}$)
455 was calculated by the time integral of the leak-subtracted Ca^{2+} current during the
456 depolarization step. ΔC_m was calculated as the difference between the average C_m before and
457 after the depolarization. To measure average C_m we used 400 ms segments and skipped the
458 initial 100 ms after the depolarization.

459

460 ## Ca^{2+} imaging

461

462 Ca^{2+} imaging was performed using spinning disc confocal microscope, as described before
463 (Ohn et al., 2016). Briefly, the set-up was equipped with a spinning disc confocal unit (CSU22,
464 Yokogawa) mounted on an upright microscope (Axio Examiner, Zeiss) and scientific CMOS
465 camera (Andor Neo). Images were acquired using 63x, 1.0 NA objective (W Plan-Apochromat,
466 Zeiss). The pixel size was measured to be 103 nm.
467 IHCs were loaded with Fluo4-FF Ca^{2+} dye and TAMRA-conjugated Ctbp2 binding dimeric
468 peptide via the patch pipette. First, the cells were scanned from bottom to top by imaging
469 TAMRA fluorescence with 561 nm laser (Jive, Cobolt AB) and exposing each plane for 0.5
470 seconds. The stack was acquired with 0.5 μm step size using Piezo positioner (Piezosystem).
471 This allowed us to identify the planes containing synaptic ribbons. Next, we recorded Fluo4-
472 FF fluorescence increase at individual synapses by imaging ribbon containing planes with 491
473 nm laser (Calypso, Cobolt AB) at 100 Hz while applying voltage ramp depolarizations to the
474 cell. 2 voltage ramps were applied at each plane, one being 5 ms shifted relative to the other.
475 Spinning disk rotation speed was set to 2000 rpm, in order to synchronize with Ca^{2+} imaging.
476 Images were analyzed using Igor Pro 6.3 (Wavemetrics). Ca^{2+} hotspots were identified by
477 subtracting the average signal of several baseline frames from the average signal of 5 frames
478 during stimulation (ΔF image). Since the same Ca^{2+} hotspot appears across multiple planes,
479 the plane exhibiting the strongest signal was chosen. The intensities of the 3x3 matrix
480 surrounding the central pixel of the hotspot were averaged across all time points to obtain the
481 intensity profiles of Ca^{2+} influx over time. Afterwards, the background signal (average of
482 approximately 60x60 pixel intensities outside the cell) was subtracted from the intensity-time
483 profiles and $\Delta F/F_0$ traces were calculated. To enhance voltage resolution of Ca^{2+} imaging, two
484 $\Delta F/F_0$ traces corresponding to two voltage ramp depolarizations (one shifted by 5 ms over the

485 other) were combined and plotted against the corresponding voltages (FV curves). These
486 curves were subsequently fitted with a modified Boltzmann function. Afterwards, fractional
487 activation curves were calculated by fitting the linear decay of the fluorescence signal from
488 the FV curves with a linear function (G_{max}) and then dividing the FV fit by the G_{max} line. The
489 resulting curves were further fitted with a Boltzmann function. Maximal Ca^{2+} influx ($\Delta F/F_{0\ max}$)
490 was calculated by averaging 5 points during the stimulation.
491
492 ## Immunohistochemistry
493
494 Amplified immunohistochemistry for NgR2 was performed on 5 μm dewaxed paraffin sections
495 of $NgR2^{+/+}$ and $NgR2^{-/-}$ inner ears from either sex. All tissue sections were incubated in 10 mM
496 sodium citrate buffer (pH = 6) at 98°C for 10 min, washed in PBS, and endogenous peroxidase
497 quenched using 3% H_2O_2, in 1X PBS for 10 min. Tissue was blocked in 2% normal goat serum,
498 1% BSA and 0.3% Triton-X100 in PBS for 2 hours at RT, followed by overnight incubation with
499 primary rabbit anti-NgR2/RTN4rl2 (1:400, Invitrogen, PA598577) at 4°C. Biotin-labelled goat
500 anti-rabbit (2 hours at RT; 1:500, Ba-1000, Vector Laboratories) and the ImmPACT DAB Kit (SK-
501 4105, Vector Laboratories) were used for signal detection. After several washes, sections were
502 incubated with TSA plus Cyanine-3 reagent (1:2000, NEL760001KT, Perkin Elmer) for 10 to
503 15 min at RT in accordance with the manufacturer's protocol. Subsequently, sections were
504 stained overnight with mouse anti-βIII-tubulin (1:1000, 801202, Biolegend) at 4°C, followed
505 by secondary Alexa Fluor 488 conjugated goat anti-mouse (1:1000, Thermo Fisher Scientific),
506 for 2 hours at RT. Finally, sections were cover slipped in Mowiol and stored at 4°C until imaging.
507 For whole mount immunofluorescence, cochleae were fixed in 4% formaldehyde on ice for
508 45-60 minutes or sometimes overnight. For anti-$Ca_V1.3$ stainings the cochleae were fixed for
509 10 minutes. After the fixation, the organs of Corti were microdissected in PBS and blocked in
510 GSDB (goat serum dilution buffer; 16% goat serum, 20 mM phosphate buffer (PB), 0.3% Triton
511 X-100, 0.45 M NaCl) for 1 hour at RT. The samples were then incubated in the primary antibody
512 mixture overnight at 4°C. The next day, samples were washed 3 times using wash buffer (20
513 mM PB, 0.3% Triton X-100, 0.45 M NaCl) followed by incubation in the secondary antibody
514 mixture for 1 hour at RT. Afterwards, the samples were washed 3 times in the washing buffer,
515 one time in PB and mounted using mounting medium (Mowiol).

516 The following primary antibodies were used: rabbit anti-Homer1 (1:500, 160 002, Synaptic
517 Systems), mouse anti-Ctbp2 (1:200, 612044, BD Biosciences), rabbit anti-$Ca_V1.3$ (1:100, ACC-
518 005, Alomone Labs), mouse anti-Bassoon (1:300, ab82958, Abcam), rabbit anti-Myosin7a
519 (1:800, ab3481, Abcam, or Proteus BioScience), guinea pig anti-RibeyeA (1:500, 192104,
520 Synaptic Systems), guinea pig anti-Synapsin1/2 (1:500, 106004, Synaptic Systems), guinea pig
521 anti-Vglut3 (1:500, 135204, Synaptic Systems), chicken anti-parvalbumin (1:200, 195006,
522 Synaptic Systems), chicken anti-calretinin (1:200, 214 106, Synaptic Systems), guinea pig anti-
523 VAChT (1:1000, 139105, Synaptic Systems), mouse anti-ATP1A3 (1:300, MA3-915, Thermo
524 Fisher Scientific).
525 The following secondary antibodies were used: Alexa Fluor 488 conjugated anti-guinea pig
526 (1:200, A11073, Thermo Fisher Scientific), Alexa Fluor 488 conjugated anti-rabbit (1:200,
527 A11008, Thermo Fisher Scientific), Alexa Fluor 568 conjugated anti-chicken (1:200, ab175711,
528 Abcam), Alexa Fluor 633 conjugated anti-guinea pig (1:200, A21105, Thermo Fisher Scientific),
529 STAR 580 conjugated anti-mouse (1:200, Abberior, ST635P-1001-500UG), STAR 635
530 conjugated anti-rabbit (1:200, Abberior, ST635P-1002-500UG).
531 Confocal stacks were acquired using Leica SP8 confocal microscope or Abberior Instruments
532 Expert Line STED microscope.
533 The volumes of the Ctbp2 and Homer1 positive puncta were estimated using the surface
534 algorithm of Imaris software (version 9.6.0, Bitplane). Following parameters were used to
535 create the surfaces for both Ctbp2 and Homer1 puncta in all the analyzed stacks: surface detail
536 0.07 μm, background subtraction 0.562 μm, touching object size 0.4 μm.
537 The brightness and the contrast of the representative images were adjusted using Fiji (ImageJ)
538 software for the visualization purposes.
539

540 ## Spiral ganglion neuron densities
541
542 $NgR2^{+/+}$ and $NgR2^{-/-}$ cochlea from p40 mice of either sex were processed for SGN counts.
543 Mouse monoclonal anti-βIII-tubulin (1:1000, 801202, Biolegend) at 4°C, followed by
544 secondary Alexa Fluor 488 conjugated anti-mouse (1:1000, Thermo Fisher Scientific), was
545 used to label all SGNs. Nuclei were visualized using a DAPI fluorescent counterstain (1:1000,
546 Life Technologies). 20X images of mid-modiolar cochlear sections were collected. ImageJ was
547 used to outline the spiral ganglion and generate the area. Quantitative assessment was

548 performed on every other mid-modiolar section to reduce chances of double counting.
549 Labeled cells were counted only if they had a round cell body, presence of nucleus, and
550 homogenous cytoplasm. Densities were calculated and statistical differences were measure
551 using a Student's t-test (GraphPad Prism, GraphPad Software Inc.).

552

553 ## Inner and outer Hair cell counts

554

555 IHC and OHC counts were performed for NgR2$^{+/+}$ and NgR2$^{-/-}$ mice at the ages of p15, 1 month
556 and 2 months. Images were imported to ImageJ software, where IHC/OHC counts were
557 performed blinded to genotype using the 'Cell counter' tool. To quantify the cells the nuclear
558 staining of the DAPI channel was used. The number of IHCs and OHCs was assessed along a
559 length of 100 μm for each image, and then averaged across all samples to obtain the average
560 number of IHCs (or OHCs) per 100 μm.

561

562 ## RNAscope

563

564 RNA *in-situ* hybridization was performed using RNAscope® (Advanced Cell Diagnostics).
565 Standard mouse probes were used to examine the expression of NgR2/RTN4rl2 (450761, ACD)
566 and Gria2 (865091, ACD) closely following the manufacturer's instructions. Briefly, 6 mm
567 paraffin tissue sections underwent deparaffinization with xylene and a series of ethanol
568 washes. Tissues were heated in kit-provided antigen retrieval buffer and digested by kit-
569 provided proteinase. Sections were exposed to mFISH target probes and incubated at 40°C in
570 a hybridization oven for 2 hours. After rinsing, mFISH signal was amplified using company-
571 provided pre-amplifier and amplifier conjugated to fluorescent dye. Subsequently, sections
572 were blocked with 1% BSA, 2% normal goat serum in 1xPBS containing 0.3% Triton X-100 for
573 1 hour at RT. The tissue was incubated in mouse anti-βIII-tubulin antibody (1:500, 801202,
574 Biolegend) overnight at 4°C. The next day, sections were rinsed with PBS, blocked again before
575 incubating in secondary Alexa Fluor 488 conjugated anti-mouse antibody (1:1000, Invitrogen)
576 for 2 hours at RT. Sections were counterstained with DAPI (1:1000, Life Technologies),
577 mounted, and stored at 4°C until image analysis. mFISH images were captured on a Leica SP8
578 confocal microscope and processed using ImageJ.

579

580

581 ## Serial block-face scanning electron microscopy (SBEM)

582

583 ### Sample preparation for SBEM

584

585 One NgR2$^{+/+}$ and two NgR2$^{-/-}$ female mice at p36 were used for the SBEM experiments.
586 Cochleae were processed for SBEM imaging as previously described (Hua et al., 2021).
587 In brief, the animals were decapitated after CO_2 inhalation under anesthesia. The cochleae
588 were dissected from the skulls and immediately fixed by perfusing with ice-cold fixative
589 through the round and oval windows at constant flow speed using an infusion pump (Micro4,
590 WPI). The fixative solution was freshly prepared and made of 4% paraformaldehyde (Sigma-
591 Aldrich), 2.5% glutaraldehyde (Sigma-Aldrich), and 0.08 M cacodylate (pH 7.4, Sigma-Aldrich).
592 After being immersed in the fixative at 4°C for 5 hours, the cochleae were transferred to a
593 decalcifying solution containing the same fixative and 5% ethylenediaminetetraacetic acid
594 (EDTA, Serva) and incubated at 4°C for 5 hours. The samples were then washed twice with
595 0.15 M cacodylate (pH 7.4) for 30 min each, sequentially immersed in 2% OsO_4 (Sigma-
596 Aldrich), 2.5% ferrocyanide (Sigma-Aldrich), and again 2% OsO_4 at RT for 2, 2, and 1.5 hours.
597 After being washed in 0.15 M cacodylate and distilled water (Sartorius) for 30 min each, the
598 samples were sequentially incubated in filtered 1% thiocarbohydrazide (TCH, Sigma-Aldrich)
599 solution and 2% OsO_4 at RT for 1 and 2 hours, as well as in lead aspartate solution (0.03 M, pH
600 5.0, adjusted with KOH) at 50 °C for 2 hours with immediate two washing steps with distilled
601 water at RT for 30 min each. For embedding, the samples were dehydrated through graded
602 pre-cooled acetone (Carl Roth) series (50%, 75%, 90%, for 30 min each, all cooled at 4 °C) and
603 then pure acetone at RT (three times for 30 min each). The sample infiltration started with 1:1
604 and 1:2 mixtures of acetone and Spurr's resin monomer (4.1 g ERL 4221, 0.95 g DER 736, 5.9
605 g NSA and 1% DMAE; Sigma-Aldrich) at RT for 6 and 12 hours on a rotator. After being
606 impregnated in pure resin for 12 hours, the samples were placed in embedding molds
607 (Polyscience) and hardened in a pre-warmed oven at 70°C for 72 hours.

608

609 ### Sample trimming and SBEM imaging

610

611 The sample blocks were mounted upright along the conical center axis on aluminum metal
612 rivets (3VMRS12, Gatan, UK) and trimmed coronally towards the modiolus using a diamond
613 trimmer (TRIM2, Leica, Germany). For each sample, a block face of about ~ 600 x 800 mm^2,

614 centered at the apical segment based on the anatomical landmarks, was created using an
615 ultramicrotome (UC7, Leica, Germany). The samples were coated with a 30 nm thick gold layer
616 using a sputter coater (ACE600, Leica, Germany). The serial images were acquired using a field-
617 emission scanning EM (Gemini300, Carl Zeiss, Germany) equipped with an in-chamber
618 ultramicrotome (3ViewXP, Gatan, UK) and back-scattered electron detector (Onpoint, Gatan,
619 UK). Focal charge compensation was set to 100 % with a high vacuum chamber pressure of
620 2.8 x 10^3 mbar. The following parameters were set for the SBEM imaging: 12 nm pixel size, 50
621 nm nominal cutting thickness, 2 keV incident beam energy, and 1.5 ms pixel dwell time.
622 For the $NgR2^{+/+}$ dataset, 2377 consecutive slices (9000 × 15000 pixels) were collected,
623 whereas the two $NgR2^{-/-}$ datasets had 3217 slices (16000 × 10000 pixels) and 2425 slices (9000
624 × 15000 pixels). All datasets were aligned along the z-direction using a custom MATLAB script
625 based on cross-correlation maximum between consecutive slices (Hua et al., 2022) before
626 being uploaded to webKnossos (Boergens et al., 2017) for skeleton and volume tracing.
627
628 ### Identification and quantification of auditory afferent fibers
629
630 In our SBEM datasets of the cochlea, manual skeleton tracing was carried out on all neurites
631 that originated from three neighboring habenula perforata (HP) at the center of each dataset.
632 To search for type I afferent fibers, several morphological features were used, such as
633 myelination after entering HP, radial and unbranched fiber trajectory, contact with IHCs, as
634 well as ribbon-associated terminals (Hua et al., 2021). This resulted in 115 putative type I
635 afferent fibers and further classification was made based on the presence of presynaptic
636 ribbon, fiber branching, and contact with IHC. For an illustration purpose, a type I afferent
637 fiber bundle of one $NgR2^{-/-}$ dataset was volume traced and 3D rendered using Amira software
638 (Thermo Scientific, US).
639
640 ### Ribbon size measurement and synapse counting
641
642 Ribbon-type synapses were manually annotated in 18 intact IHCs captured by SBEM using
643 webKnossos. The dense core region of individual ribbon synapses was manually contoured,
644 and the associated voxels were counted for ribbon volume measurement. In the case of multi-
645 ribbon synapses, all ribbon bodies at a single active zone were summed up to yield the ribbon
646 volume.

Auditory brainstem responses

Auditory brainstem resposes (ABR) were recorded in 2-4 months old mice of either sex, as described previously (Luque et al., 2021). Briefly, we used a custom-made system in an anechoic chamber in a calibrated open-field configuration. ABRs were recorded via needle electrodes in response to tone bursts of 4, 8, 16, and 32 kHz or a click wide spectrum (2-45,2 KHz, 2 KHz steps) as stimuli. Tone pips of 3 ms duration (1 ms rise and fall time) were presented at a rate of 60/s with alternating phases. Starting with 0 dB, the stimuli were increased in 5 dB steps up to 120 dB. Hearing thresholds were determined as the minimum stimulation level that produced a clearly recognizable potential. Recordings were evaluated by three independent researchers in a blinded manner.

Data analysis and statistics

The data were analyzed using Igor Pro (Wavemetrics), Python and GraphPad Prism (GraphPad Software Inc.) software. For 2 sample comparisons, data were tested for normality and equality of variances using Jarque-Bera and F-test, respectively. Afterwards, two-tailed Student's t-test or Mann-Whitney-Wilcoxon test were performed. The latter was used when normality and/or equality of variances were not met. P-values were corrected for multiple comparisons using Holm-Šídák method. For ABR thresholds Kruskal-Wallis test followed by Dunn's multiple comparison test was used. Data is presented as mean ± standard error of the mean (SEM), unless otherwise stated. Significances are reported as *$p < 0.05$, **$p < 0.01$, ***$p < 0.001$. The number of the animals is indicated as N.

Acknowledgements

We thank Sina Langer, Christiane Senger-Freitag, Sandra Gerke for expert technical support. We thank Prof. Dr. Carolin Wichmann, Dr. Susann Michanski, Julius Bahr and Sophia Mutschall for the help with the SBEM sample preparation. We thank Dr. Yi Jiang and Haoyu Wang for the visualization of neurite reconstruction. We would also like to thank Prof. Dr. Olaf Jahn and Lars van Werven for the TAMRA-conjugated Ctbp2 binding peptide synthesis. The study was supported by German Research Foundation through the Cluster of Excellence (EXC2067) Multiscale Bioimaging (TM) and the Leibniz Program (MO896/5 to TM) as well as by the

European Research Council through the Advanced Grant “DynaHear” to TM under the European Union’s Horizon 2020 Research and Innovation program (grant agreement No. 101054467), and by Fondation Pour l’Audition (FPA RD-2020-10), by the SPIN-FWF grant to CB, and by the National Natural Science Foundation of China (82171133 to YH), Industrial Support Fund of Huangpu District .in Shanghai (XK2019011 to YH), Innovative Research Team of High-level Local Universities in Shanghai (SHSMU-ZLCX20211700). NK is a member of the Hertha Sponer College from the Cluster of Excellence Multiscale Bioimaging (MBExC). TM is a Max-Planck Fellow at the Max Planck Institute for Multidisciplinary Sciences.

Author contributions

CB, TM, YH, and NK designed the research. NK, MÜ, YQ, NB, FH, LJC, FW, ML, RG performed experiments and analyzed data. NK and TM wrote the paper with contributions of YH, CB, YQ, NB. CB, TM, YH acquired funding. All authors have reviewed and approved the final version of the manuscript for submission.

References

Appler, J. M., and Goodrich, L. V. (2011). Connecting the ear to the brain: Molecular mechanisms of auditory circuit assembly. *Prog. Neurobiol.* 93, 488–508. doi: 10.1016/j.pneurobio.2011.01.004

Bäumer, B. E., Kurz, A., Borrie, S. C., Sickinger, S., Dours-Zimmermann, M. T., Zimmermann, D. R., et al. (2014). Nogo receptor homolog NgR2 expressed in sensory DRG neurons controls epidermal innervation by interaction with Versican. *J. Neurosci. Off. J. Soc. Neurosci.* 34, 1633–1646. doi: 10.1523/JNEUROSCI.3094-13.2014

Boergens, K. M., Berning, M., Bocklisch, T., Bräunlein, D., Drawitsch, F., Frohnhofen, J., et al. (2017). webKnossos: efficient online 3D data annotation for connectomics. *Nat. Methods* 14, 691–694. doi: 10.1038/nmeth.4331

Borrie, S. C., Sartori, S. B., Lehmann, J., Sah, A., Singewald, N., and Bandtlow, C. E. (2014). Loss of Nogo receptor homolog NgR2 alters spine morphology of CA1 neurons and emotionality in adult mice. *Front. Behav. Neurosci.* 8. Available at: https://www.frontiersin.org/articles/10.3389/fnbeh.2014.00175 (Accessed March 1, 2024).

Bulankina, A. V., and Moser, T. (2012). Neural circuit development in the mammalian cochlea. *Physiology* 27, 100–112. doi: 10.1152/physiol.00036.2011

Cantu-Guerra, H. L., Papazian, M. R., Gorsky, A. L., Alekos, N. S., Caccavano, A., Karagulyan, N., et al. (2023). Cochlear hair cell innervation is dependent on a modulatory function of SEMAPHORIN-3A. *Dev. Dyn.* 252, 124–144. doi: 10.1002/dvdy.548

Carlton, A. J., Jeng, J.-Y., Grandi, F. C., De Faveri, F., Amariutei, A. E., De Tomasi, L., et al. (2024). BAI1 localizes AMPA receptors at the cochlear afferent post-synaptic density and is essential for hearing. *Cell Rep.* 43, 114025. doi: 10.1016/j.celrep.2024.114025

Coate, T. M., Scott, M. K., and Gurjar, M. (2019). Current concepts in cochlear ribbon synapse formation. *Synapse* 73, e22087. doi: 10.1002/syn.22087

Coate, T. M., Spita, N. A., Zhang, K. D., Isgrig, K. T., and Kelley, M. W. (2015). Neuropilin-2/Semaphorin-3F-mediated repulsion promotes inner hair cell innervation by spiral ganglion neurons. *eLife* 4. doi: 10.7554/eLife.07830

Defourny, J., Poirrier, A.-L., Lallemend, F., Mateo Sánchez, S., Neef, J., Vanderhaeghen, P., et al. (2013). Ephrin-A5/EphA4 signalling controls specific afferent targeting to cochlear hair cells. *Nat. Commun.* 4, 1438. doi: 10.1038/ncomms2445

Domeniconi, M., Cao, Z., Spencer, T., Sivasankaran, R., Wang, K. C., Nikulina, E., et al. (2002). Myelin-Associated Glycoprotein Interacts with the Nogo66 Receptor to Inhibit Neurite Outgrowth. *Neuron* 35, 283–290. doi: 10.1016/S0896-6273(02)00770-5

Elkon, R., Milon, B., Morrison, L., Shah, M., Vijayakumar, S., Racherla, M., et al. (2015). RFX transcription factors are essential for hearing in mice. *Nat. Commun.* 6, 8549. doi: 10.1038/ncomms9549

Fell, B., Eckrich, Stephanie, Hecker, Dietmar, Obermair, Gerald J., Flockerzi, V., Schick, B., et al. (2015). α2δ2 Controls the Function and Transsynaptic Coupling of Cav1.3 Channels in Mouse Inner Hair Cells and is Essential for Normal Hearing. *ARO Midwintermeeting*.

Fournier, A. E., GrandPre, T., and Strittmatter, S. M. (2001). Identification of a receptor mediating Nogo-66 inhibition of axonal regeneration. *Nature* 409, 341–346. doi: 10.1038/35053072

Hua, Y., Ding, X., Wang, H., Wang, F., Lu, Y., Neef, J., et al. (2021). Electron Microscopic Reconstruction of Neural Circuitry in the Cochlea. *Cell Rep.* 34, 108551. doi: 10.1016/j.celrep.2020.108551

Hua, Y., Loomba, S., Pawlak, V., Voit, K.-M., Laserstein, P., Boergens, K. M., et al. (2022). Connectomic analysis of thalamus-driven disinhibition in cortical layer 4. *Cell Rep.* 41, 111476. doi: 10.1016/j.celrep.2022.111476

Jaime Tobón, L. M., and Moser, T. (2023a). Bridging the gap between presynaptic hair cell function and neural sound encoding. doi: 10.7554/eLife.93749.1

Jaime Tobón, L. M., and Moser, T. (2023b). Ca2+ regulation of glutamate release from inner hair cells of hearing mice. *Proc. Natl. Acad. Sci.* 120, e2311539120. doi: 10.1073/pnas.2311539120

Jean, P., Morena, D. L. de la, Michanski, S., Tobón, L. M. J., Chakrabarti, R., Picher, M. M., et al. (2018). The synaptic ribbon is critical for sound encoding at high rates and with temporal precision. *eLife* 7, e29275. doi: 10.7554/eLife.29275

Jean, P., Wong Jun Tai, F., Singh-Estivalet, A., Lelli, A., Scandola, C., Megharba, S., et al. (2023). Single-cell transcriptomic profiling of the mouse cochlea: An atlas for targeted therapies. *Proc. Natl. Acad. Sci.* 120, e2221744120. doi: 10.1073/pnas.2221744120

Johnson, S. L., Safieddine, S., Mustapha, M., and Marcotti, W. (2019). Hair Cell Afferent Synapses: Function and Dysfunction. *Cold Spring Harb. Perspect. Med.* 9. doi: 10.1101/cshperspect.a033175

Jukic, A., Lei, Z., Cebul, E. R., Pinter, K., Mosqueda, N., David, S., et al. (2024). Presynaptic Nrxn3 is essential for ribbon-synapse assembly in hair cells. doi: 10.1101/2024.02.14.580267

Jung, J. S., Zhang, K. D., Wang, Z., McMurray, M., Tkaczuk, A., Ogawa, Y., et al. (2019). Semaphorin-5B Controls Spiral Ganglion Neuron Branch Refinement during Development. *J. Neurosci.* 39, 6425–6438. doi: 10.1523/JNEUROSCI.0113-19.2019

Koundakjian, E. J., Appler, J. L., and Goodrich, L. V. (2007). Auditory neurons make stereotyped wiring decisions before maturation of their targets. *J. Neurosci. Off. J. Soc. Neurosci.* 27, 14078–14088. doi: 10.1523/JNEUROSCI.3765-07.2007

Kujawa, S. G., and Liberman, M. C. (2009). Adding insult to injury: cochlear nerve degeneration after “temporary” noise-induced hearing loss. *J. Neurosci.* 29, 14077.

Kujawa, S. G., and Liberman, M. C. (2015). Synaptopathy in the noise-exposed and aging cochlea: Primary neural degeneration in acquired sensorineural hearing loss. *Hear. Res.* 330, 191–199. doi: 10.1016/j.heares.2015.02.009

Kwiatkowska, M., Reinhard, J., Roll, L., Kraft, N., Dazert, S., Faissner, A., et al. (2016). The expression pattern and inhibitory influence of Tenascin-C on the growth of spiral ganglion neurons suggest a regulatory role as boundary formation molecule in the postnatal mouse inner ear. *Neuroscience* 319, 46–58. doi: 10.1016/j.neuroscience.2016.01.039

Liberman, L. D., and Liberman, M. C. (2016). Postnatal maturation of auditory-nerve heterogeneity, as seen in spatial gradients of synapse morphology in the inner hair cell area. *Hear. Res.* 339, 12–22. doi: 10.1016/j.heares.2016.06.002

Lindau, M., and Neher, E. (1988). Patch-clamp techniques for time-resolved capacitance measurements in single cells. *Pflüg. Arch. Eur. J. Physiol.* 411, 137–146.

Liu, H., Chen, L., Giffen, K. P., Stringham, S. T., Li, Y., Judge, P. D., et al. (2018). Cell-Specific Transcriptome Analysis Shows That Adult Pillar and Deiters’ Cells Express Genes Encoding Machinery for Specializations of Cochlear Hair Cells. *Front. Mol. Neurosci.* 11. doi: 10.3389/fnmol.2018.00356

Lu, Y., Liu, J., Li, B., Wang, H., Wang, F., Wang, S., et al. (2024). Spatial patterns of noise-induced inner hair cell ribbon loss in the mouse mid-cochlea. *iScience* 27, 108825. doi: 10.1016/j.isci.2024.108825

Luque, M., Schrott-Fischer, A., Dudas, J., Pechriggl, E., Brenner, E., Rask-Andersen, H., et al. (2021). HCN channels in the mammalian cochlea: Expression pattern, subcellular location, and age-dependent changes. *J. Neurosci. Res.* 99, 699–728. doi: 10.1002/jnr.24754

Matsubara, A., Laake, J. H., Davanger, S., Usami, S., and Ottersen, O. P. (1996). Organization of AMPA receptor subunits at a glutamate synapse: a quantitative immunogold analysis of hair cell synapses in the rat organ of Corti. *J. Neurosci.* 16, 4457.

Meyer, A. C., and Moser, T. (2010). Structure and function of cochlear afferent innervation. *Curr. Opin. Otolaryngol. Head Neck Surg.* 18, 441–446. doi: 10.1097/MOO.0b013e32833e0586

Michanski, S., Smaluch, K., Steyer, A. M., Chakrabarti, R., Setz, C., Oestreicher, D., et al. (2019). Mapping developmental maturation of inner hair cell ribbon synapses in the

806 apical mouse cochlea. *Proc. Natl. Acad. Sci.* 116, 6415–6424. doi:
807 10.1073/pnas.1812029116

808 Mironova, Y. A., and Giger, R. J. (2013). Where no synapses go: gatekeepers of circuit
809 remodeling and synaptic strength. *Trends Neurosci.* 36, 363–373. doi:
810 10.1016/j.tins.2013.04.003

811 Moser, T., and Beutner, D. (2000). Kinetics of exocytosis and endocytosis at the cochlear
812 inner hair cell afferent synapse of the mouse. *Proc. Natl. Acad. Sci.* 97, 883–888. doi:
813 10.1073/pnas.97.2.883

814 Moverman, D. J., Liberman, L. D., Kraemer, S., Corfas, G., and Liberman, M. C. (2023).
815 Ultrastructure of noise-induced cochlear synaptopathy. *Sci. Rep.* 13, 19456. doi:
816 10.1038/s41598-023-46859-6

817 Niedzielski, A. S., and Wenthold, R. J. (1995). Expression of AMPA, kainate, and NMDA
818 receptor subunits in cochlear and vestibular ganglia. *J. Neurosci.* 15, 2338.

819 Ohn, T.-L., Rutherford, M. A., Jing, Z., Jung, S., Duque-Afonso, C. J., Hoch, G., et al. (2016).
820 Hair cells use active zones with different voltage dependence of Ca^{2+} influx to
821 decompose sounds into complementary neural codes. *Proc. Natl. Acad. Sci.* 113,
822 E4716–E4725. doi: 10.1073/pnas.1605737113

823 Özçete, Ö. D., and Moser, T. (2021). A sensory cell diversifies its output by varying Ca^{2+} influx-
824 release coupling among active zones. *EMBO J.* 40, e106010. doi:
825 10.15252/embj.2020106010

826 Ramirez, M. A., Ninoyu, Y., Miller, C., Andrade, L. R., Edassery, S., Bomba-Warczak, E., et al.
827 (2022). Cochlear ribbon synapse maturation requires Nlgn1 and Nlgn3. *iScience* 25,
828 104803. doi: 10.1016/j.isci.2022.104803

829 Roux, I., Safieddine, S., Nouvian, R., Grati, M., Simmler, M.-C., Bahloul, A., et al. (2006).
830 Otoferlin, Defective in a Human Deafness Form, Is Essential for Exocytosis at the
831 Auditory Ribbon Synapse. *Cell* 127, 277–289. doi: 10.1016/j.cell.2006.08.040

832 Ruel, J., Emery, S., Nouvian, R., Bersot, T., Amilhon, B., Van Rybroek, J. M., et al. (2008).
833 Impairment of SLC17A8 Encoding Vesicular Glutamate Transporter-3, VGLUT3,
834 Underlies Nonsyndromic Deafness DFNA25 and Inner Hair Cell Dysfunction in Null
835 Mice. *Am. J. Hum. Genet.* 83, 278–292. doi: 10.1016/j.ajhg.2008.07.008

836 Rutherford, M. A., Bhattacharyya, A., Xiao, M., Cai, H.-M., Pal, I., and Rubio, M. E. (2023).
837 GluA3 subunits are required for appropriate assembly of AMPAR GluA2 and GluA4
838 subunits on cochlear afferent synapses and for presynaptic ribbon modiolar-pillar
839 morphology. *eLife* 12, e80950. doi: 10.7554/eLife.80950

840 Schwab, M. E. (2010). Functions of Nogo proteins and their receptors in the nervous system.
841 *Nat. Rev. Neurosci.* 11, 799–811. doi: 10.1038/nrn2936

842 Seal, R. P., Akil, O., Yi, E., Weber, C. M., Grant, L., Yoo, J., et al. (2008). Sensorineural Deafness
843 and Seizures in Mice Lacking Vesicular Glutamate Transporter 3. *Neuron* 57, 263–275.
844 doi: 10.1016/j.neuron.2007.11.032

845 Sherrill, H. E., Jean, P., Driver, E. C., Sanders, T. R., Fitzgerald, T. S., Moser, T., et al. (2019).
846 Pou4f1 Defines a Subgroup of Type I Spiral Ganglion Neurons and Is Necessary for
847 Normal Inner Hair Cell Presynaptic Ca2+ Signaling. *J. Neurosci.* 39, 5284–5298. doi:
848 10.1523/JNEUROSCI.2728-18.2019

849 Shrestha, B. R., Chia, C., Wu, L., Kujawa, S. G., Liberman, M. C., and Goodrich, L. V. (2018).
850 Sensory Neuron Diversity in the Inner Ear Is Shaped by Activity. *Cell* 174, 1229-
851 1246.e17. doi: 10.1016/j.cell.2018.07.007

852 Shrestha, B. R., Wu, L., and Goodrich, L. V. (2023). Runx1 controls auditory sensory neuron
853 diversity in mice. *Dev. Cell* 58, 306-319.e5. doi: 10.1016/j.devcel.2023.01.008

854 Sonntag, M., Blosa, M., Schmidt, S., Reimann, K., Blum, K., Eckrich, T., et al. (2018). Synaptic
855 coupling of inner ear sensory cells is controlled by brevican-based extracellular
856 matrix baskets resembling perineuronal nets. *BMC Biol.* 16, 99. doi: 10.1186/s12915-
857 018-0566-8

858 Vaccaro, G., Dumoulin, A., Zuñiga, N. R., Bandtlow, C. E., and Stoeckli, E. T. (2022). The Nogo-
859 66 Receptors NgR1 and NgR3 Are Required for Commissural Axon Pathfinding. *J.*
860 *Neurosci.* 42, 4087–4100. doi: 10.1523/JNEUROSCI.1390-21.2022

861 Venkatesh, K., Chivatakarn, O., Lee, H., Joshi, P. S., Kantor, D. B., Newman, B. A., et al. (2005).
862 The Nogo-66 Receptor Homolog NgR2 Is a Sialic Acid-Dependent Receptor Selective
863 for Myelin-Associated Glycoprotein. *J. Neurosci.* 25, 808–822. doi:
864 10.1523/JNEUROSCI.4464-04.2005

865 Wang, J., Miao, Y., Wicklein, R., Sun, Z., Wang, J., Jude, K. M., et al. (2021). RTN4/NoGo-
866 receptor binding to BAI adhesion-GPCRs regulates neuronal development. *Cell* 184,
867 5869-5885.e25. doi: 10.1016/j.cell.2021.10.016

868 Wang, K. C., Koprivica, V., Kim, J. A., Sivasankaran, R., Guo, Y., Neve, R. L., et al. (2002).
869 Oligodendrocyte-myelin glycoprotein is a Nogo receptor ligand that inhibits neurite
870 outgrowth. *Nature* 417, 941–944. doi: 10.1038/nature00867

871 Wills, Z. P., Mandel-Brehm, C., Mardinly, A. R., McCord, A. E., Giger, R. J., and Greenberg, M.
872 E. (2012). The Nogo Receptor Family Restricts Synapse Number in the Developing
873 Hippocampus. *Neuron* 73, 466–481. doi: 10.1016/j.neuron.2011.11.029

874 Wong, A. B., Rutherford, M. A., Gabrielaitis, M., Pangršič, T., Göttfert, F., Frank, T., et al.
875 (2014). Developmental refinement of hair cell synapses tightens the coupling of Ca2+
876 influx to exocytosis. *EMBO J.* 33, 247–264. doi: 10.1002/embj.201387110

877 Wörter, V., Schweigreiter, R., Kinzel, B., Mueller, M., Barske, C., Böck, G., et al. (2009).
878 Inhibitory activity of myelin-associated glycoprotein on sensory neurons is largely

879 independent of NgR1 and NgR2 and resides within Ig-Like domains 4 and 5. *PloS One*
880 4, e5218. doi: 10.1371/journal.pone.0005218

881 Zenisek, D., Horst, N. K., Merrifield, C., Sterling, P., and Matthews, G. (2004). Visualizing
882 synaptic ribbons in the living cell. *J. Neurosci. Off. J. Soc. Neurosci.* 24, 9752–9759.
883 doi: 10.1523/JNEUROSCI.2886-04.2004

884

Supplementary Figures

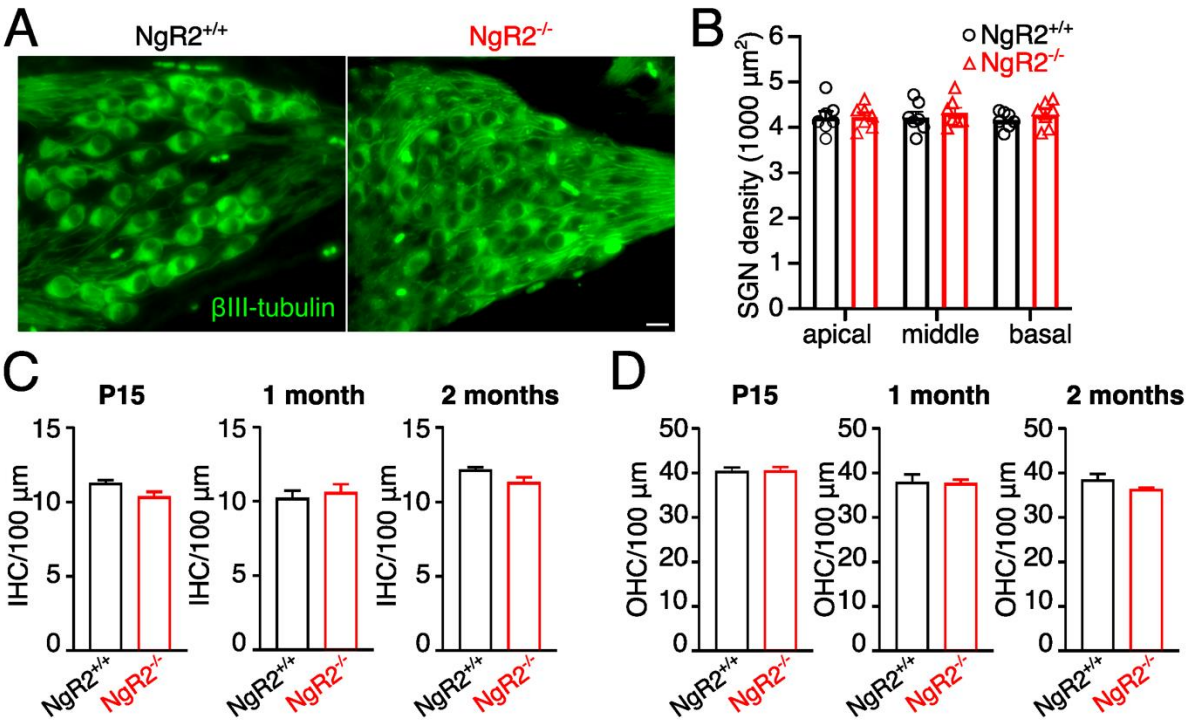

Figure 2-figure supplement 1. Cell densities are not changed in NgR2$^{-/-}$ cochleae. (**A**) Mid/Basal-modiolar sections labeled for βIII-tubulin (green, neurons) from p40 NgR2$^{+/+}$ and NgR2$^{-/-}$ mice Exemplary section for NgR2$^{-/-}$ is the zoomed out image presented in figure 1C. (**B**) Quantitative analysis shows that the density of SGN cell bodies are similar between NgR2$^{-/-}$ and control cochlea. Data is presented as mean ± SD; N = 7 per group. Scale bar = 10 µm. (**C, D**) IHC (C) and OHC (D) densities are not affected in P15, 1 month and 2 months old NgR2$^{-/-}$ mice.

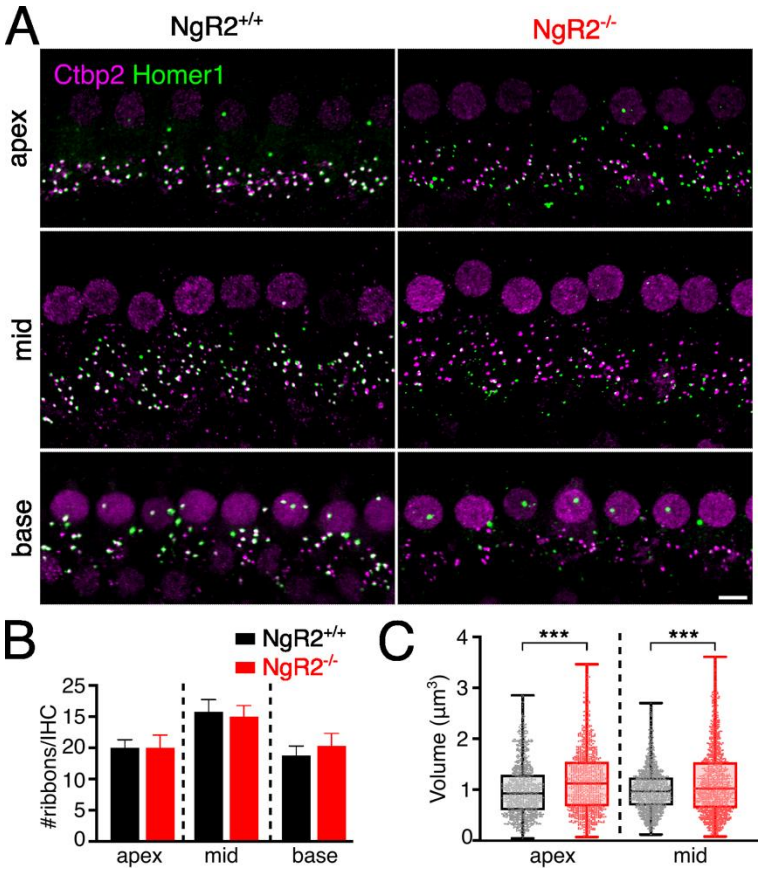

Figure 2-figure supplement 2. Intact number but enlarged size of the ribbons in NgR2$^{-/-}$ IHCs. (**A**) Maximal intensity projections of representative IHCs from apical, mid and basal regions of NgR2$^{+/+}$ (left) and NgR2$^{-/-}$ (right) cochleae of p21-30 mice. Synapses are visualized by staining against Ctbp2 and Homer1. Scale bar = 5 µm. (**B**) The number of the ribbons is not affected along the tonotopic axis in NgR2$^{-/-}$ cochleae. (**C**) The size of the ribbons is increased in IHCs of both apical and middle turns in NgR2$^{-/-}$ cochleae. N = 6 animals/genotype. Box-whisker plots show the median, 25/75 percentiles (box) and the range (whiskers). Individual data points are overlaid.

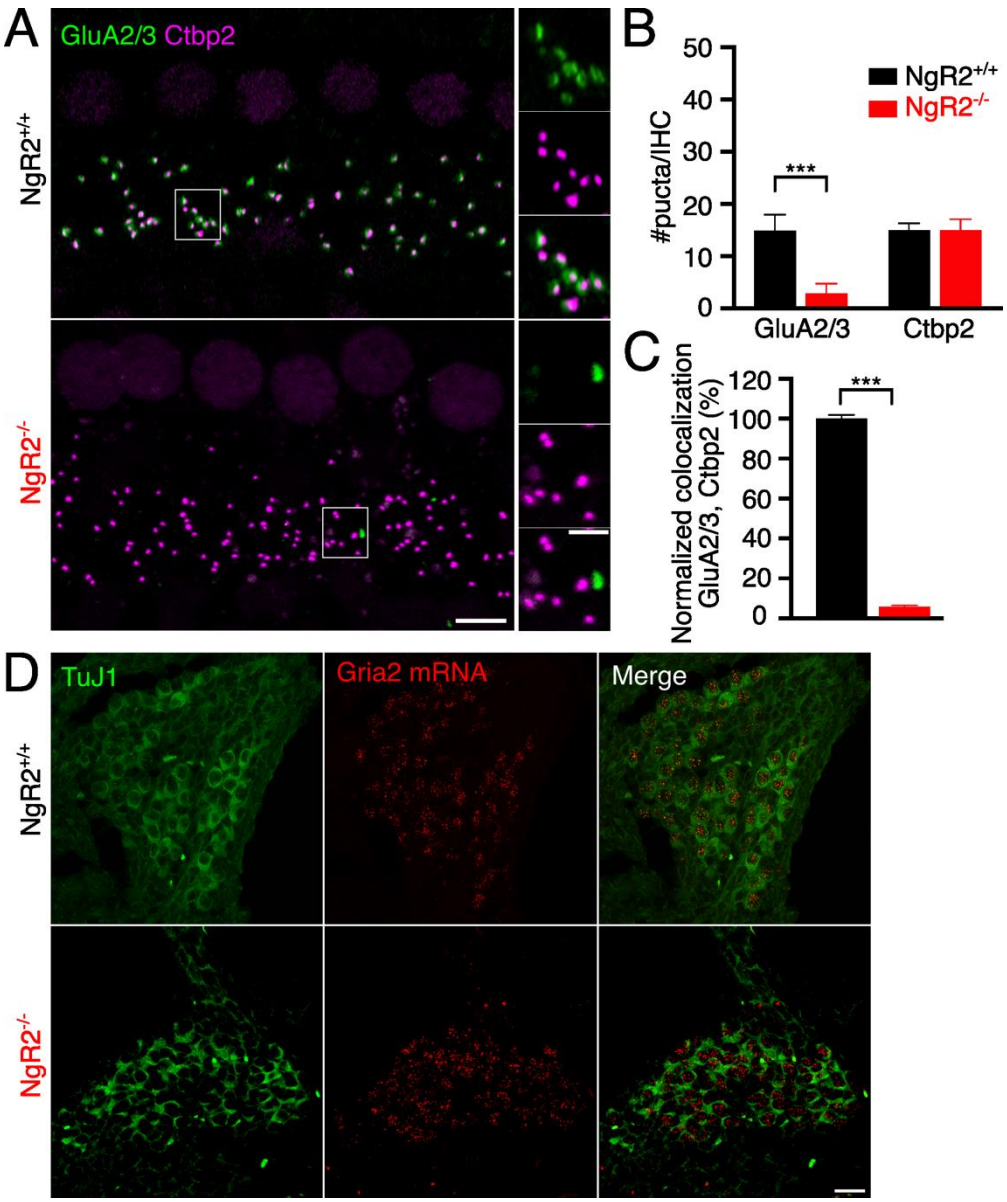

Figure 2-figure supplement 3. Reduced GluA2/3 signal juxtaposing presynaptic ribbons in IHCs of NgR2$^{-/-}$ mice. (**A**) Maximal intensity projections of representative IHC regions from NgR2$^{+/+}$ (top) and NgR2$^{-/-}$ (bottom) cochleae immunolabeled against Ctbp2 and GluA2/3. Scale bar = 5 μm. The zoom-in regions marked with the white rectagles are presented on the right-hand side. Scale bar = 2 μm. (**B**) The number of the GluA2/3 positive puncta is drastically reduced in NgR2$^{-/-}$ mice despite the maintained number of presynaptic ribbons. (**C**) Disrupted colocalization of Ctbp2 and GluA2 positive puncta at IHCs of NgR2$^{-/-}$ mice. N = 6 animals/genotype. (**D**) Representative images of RNAscope ISH show maintained expression of Gria2 (red dots) in the SGN somata of NgR2$^{-/-}$ mice. Scale bar = 10 μm.

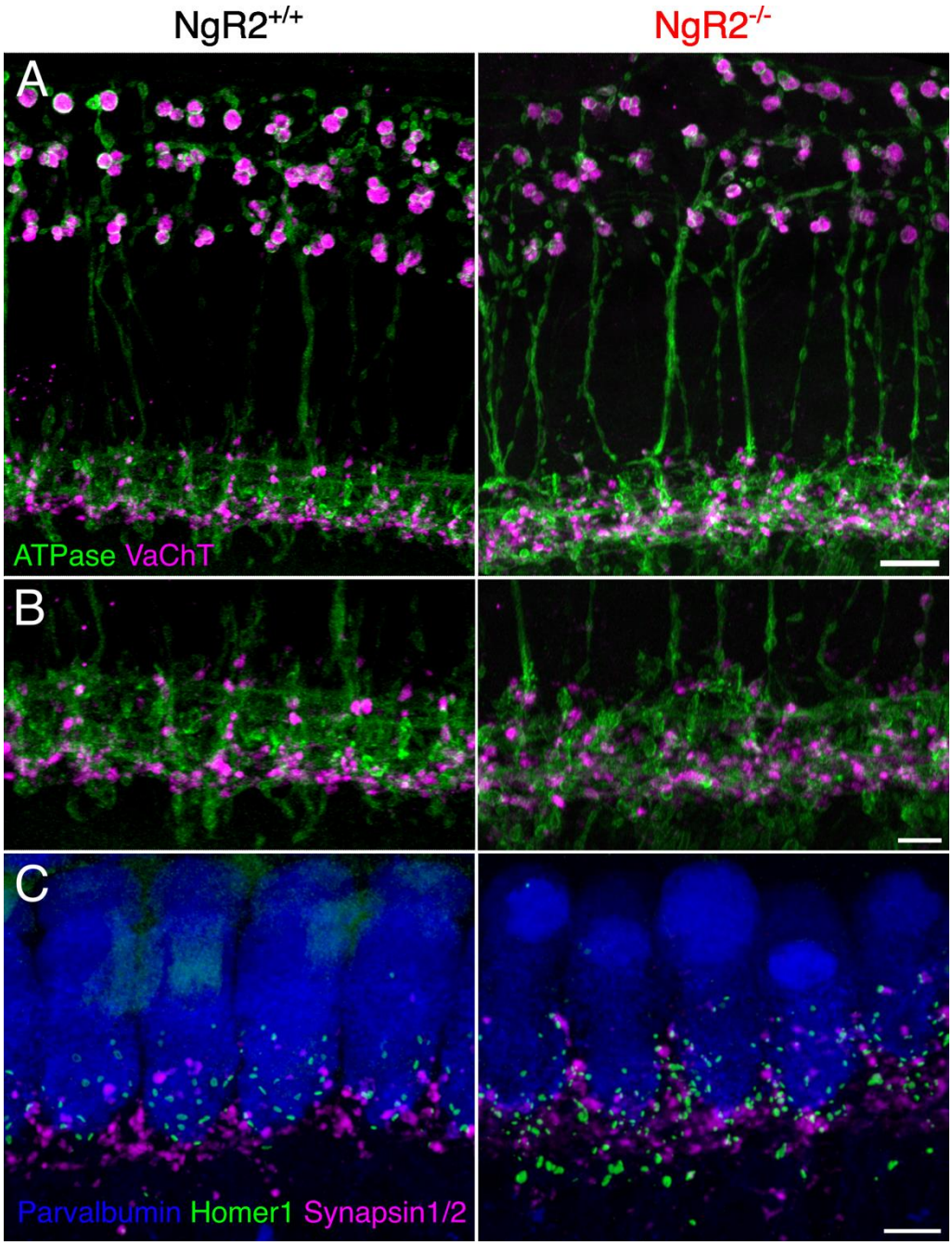

Figure 2-figure supplement 4. Efferent innervation pattern in NgR2$^{-/-}$ cochleae. (**A**) Maximal intensity projections of confocal stacks of outer and inner hair cell regions at the apical region of the cochlea from p21-30 NgR2$^{+/+}$ (left) and NgR2$^{-/-}$ (right) mice. SGN fibers/terminals and efferent terminals are visualized using anti-Na^{2+}/K^{+} ATPase and anti-vesicular acetylcholine transporter (VaChT) antibodies, respectively. Scale Bar = 10 µm (**B**) Same as A but zoomed into the IHC region. Scale Bar = 5 µm (**C**) Maximal intensity projections of confocal stacks of a row of apical IHC region from p21 NgR2$^{+/+}$ (left) and NgR2$^{-/-}$ (right) mice. Presynaptic efferent terminals were stained with anti-synapsin1/2 antibody. Scale bar = 5 µm.

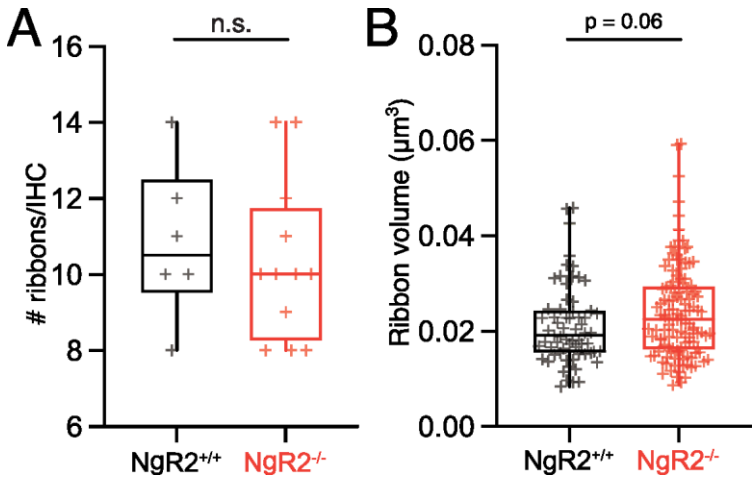

Figure 3-figure supplement 1. Quantification of ribbon number and volume in SBEM reconstructions. (**A**) Number of ribbons is not changed in NgR2$^{-/-}$ IHCs (NgR2$^{+/+}$: 10.8 ± 0.83, SD = 2.04, n = 6, N = 1 vs NgR2$^{-/-}$: 10.3 ± 0.61, SD = 2.1, n = 12, N = 2; p = 0.54, Mann-Whitney-Wilcoxon test). (**B**) Ribbon volume tends to be larger in NgR2$^{-/-}$ IHCs (NgR2$^{+/+}$: 0.021 ± 0.001 µm^3, SD = 0.008 µm^3, n = 65 ribbons in 6 IHCs, N = 1 vs NgR2$^{-/-}$: 0.024 ± 0.001 µm^3, SD = 0.01 µm^3, n = 125 ribbons in 12 IHCs, N = 2; p = 0.06, Mann-Whitney-Wilcoxon test). Box-whisker plots show the median, 25/75 percentiles (box) and the range (whiskers). Individual data points are overlaid.

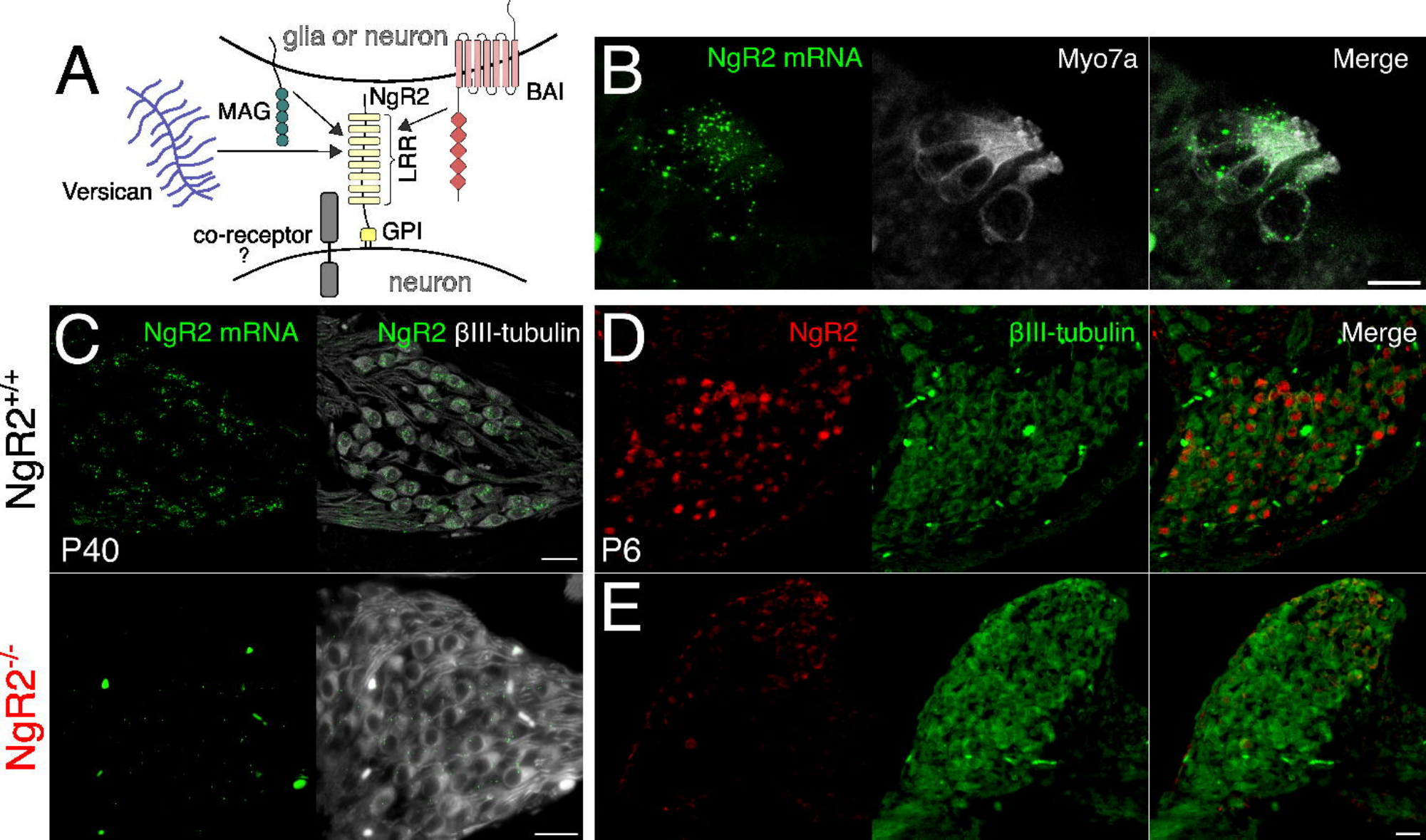
A
glia or neuron
BAI
MAG
NgR2
LRR
Versican
co-receptor
?
GPI
neuron
B
NgR2 mRNA
Myo7a
Merge
C
NgR2 mRNA
NgR2 βIII-tubulin
P40
D
NgR2
βIII-tubulin
Merge
P6
E
NgR2+/+
NgR2-/-

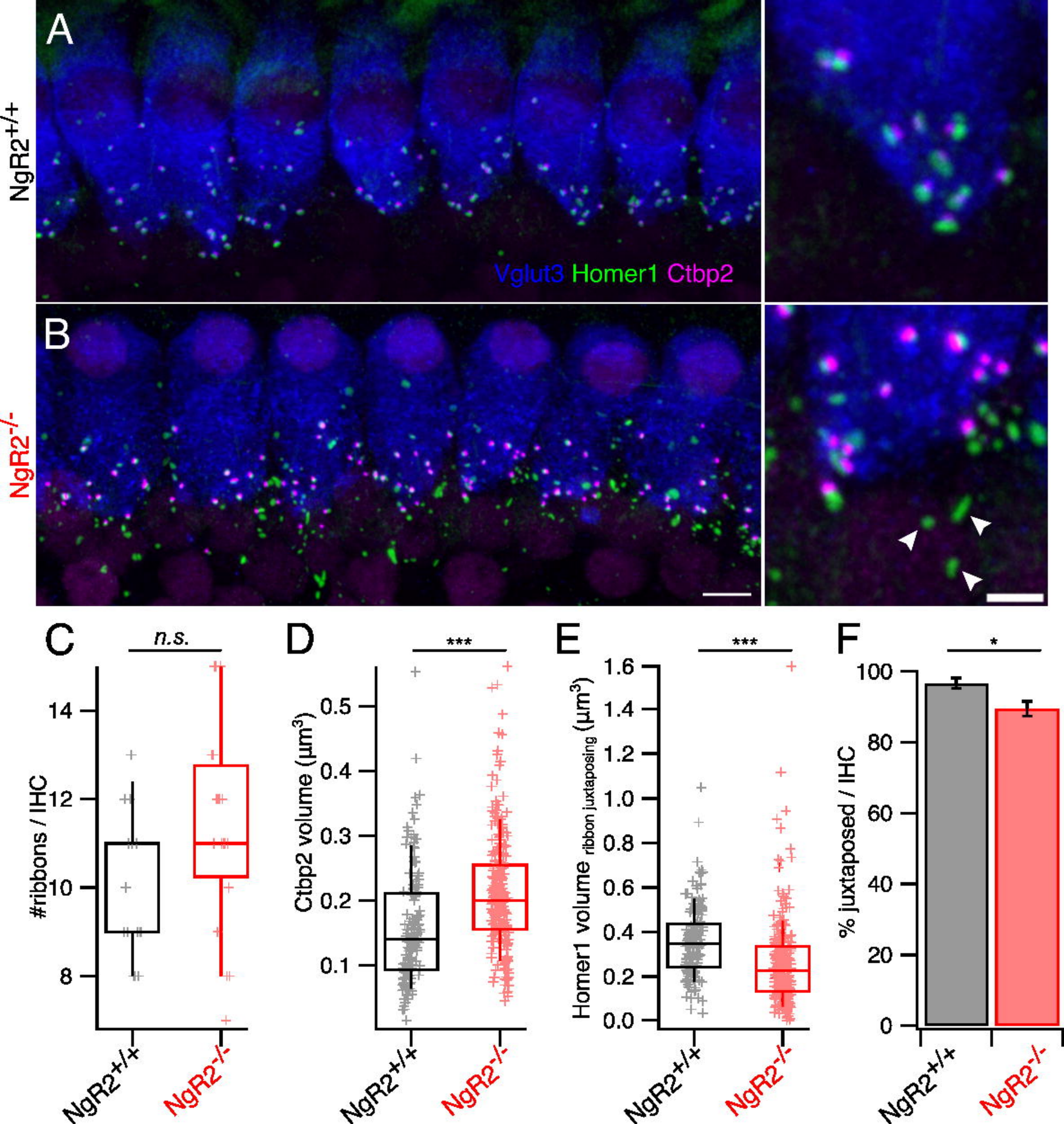
A
B
NgR2+/+
NgR2-/-
Vglut3 Homer1 Ctbp2
C
n.s.
#ribbons / IHC
D
***
Ctbp2 volume (µm3)
E
***
Homer1 volume ribbon juxtaposing (µm3)
F
*
% juxtaposed / IHC
NgR2+/+
NgR2-/-

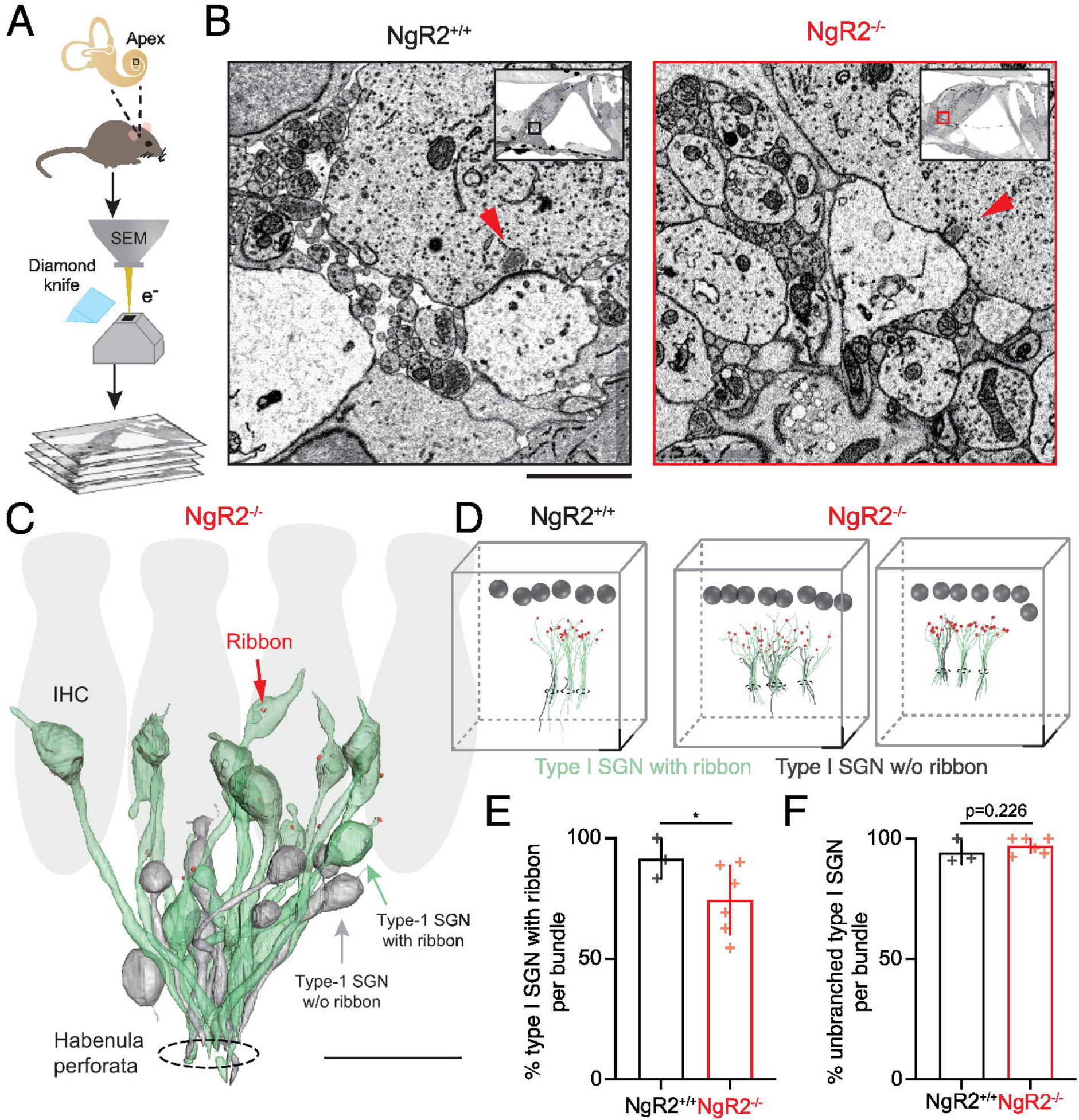
A
Apex
SEM
Diamond knife
e⁻
B
NgR2+/+
NgR2-/-
C
NgR2-/-
Ribbon
IHC
Type-1 SGN with ribbon
Type-1 SGN w/o ribbon
Habenula perforata
D
NgR2+/+
NgR2-/-
Type I SGN with ribbon
Type I SGN w/o ribbon
E
*
% type I SGN with ribbon per bundle
100
50
0
NgR2+/+
NgR2-/-
F
p=0.226
% unbranched type I SGN per bundle
100
50
0
NgR2+/+
NgR2-/-

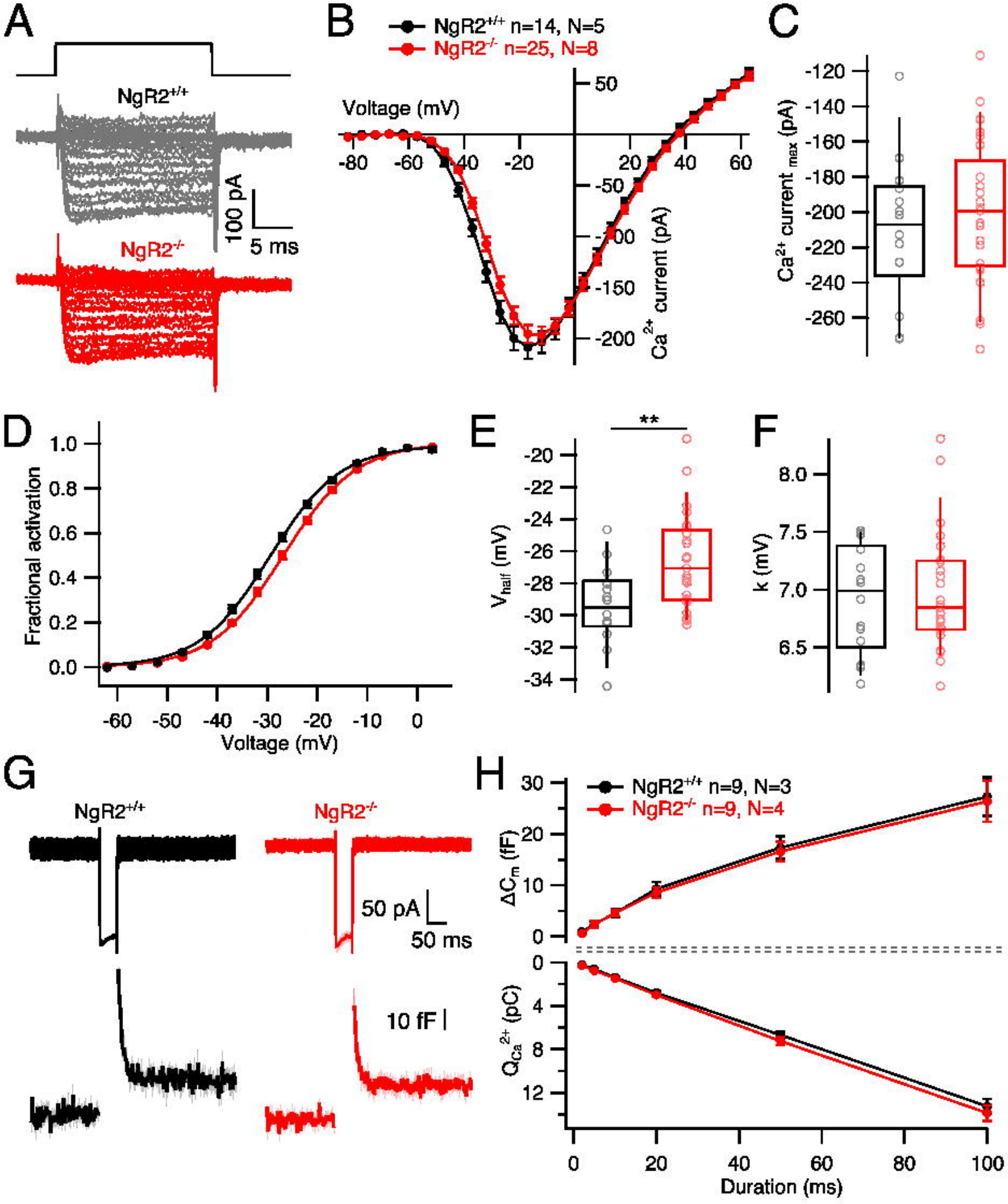
A
NgR2+/+
NgR2-/-
100 pA
5 ms
B
NgR2+/+ n=14, N=5
NgR2-/- n=25, N=8
Voltage (mV)
Ca2+ current (pA)
C
Ca2+ current max (pA)
D
Fractional activation
Voltage (mV)
E
Vhalf (mV)
**
F
k (mV)
G
NgR2+/+
NgR2-/-
50 pA
50 ms
10 fF
H
NgR2+/+ n=9, N=3
NgR2-/- n=9, N=4
ΔCm (fF)
QCa2+ (pC)
Duration (ms)

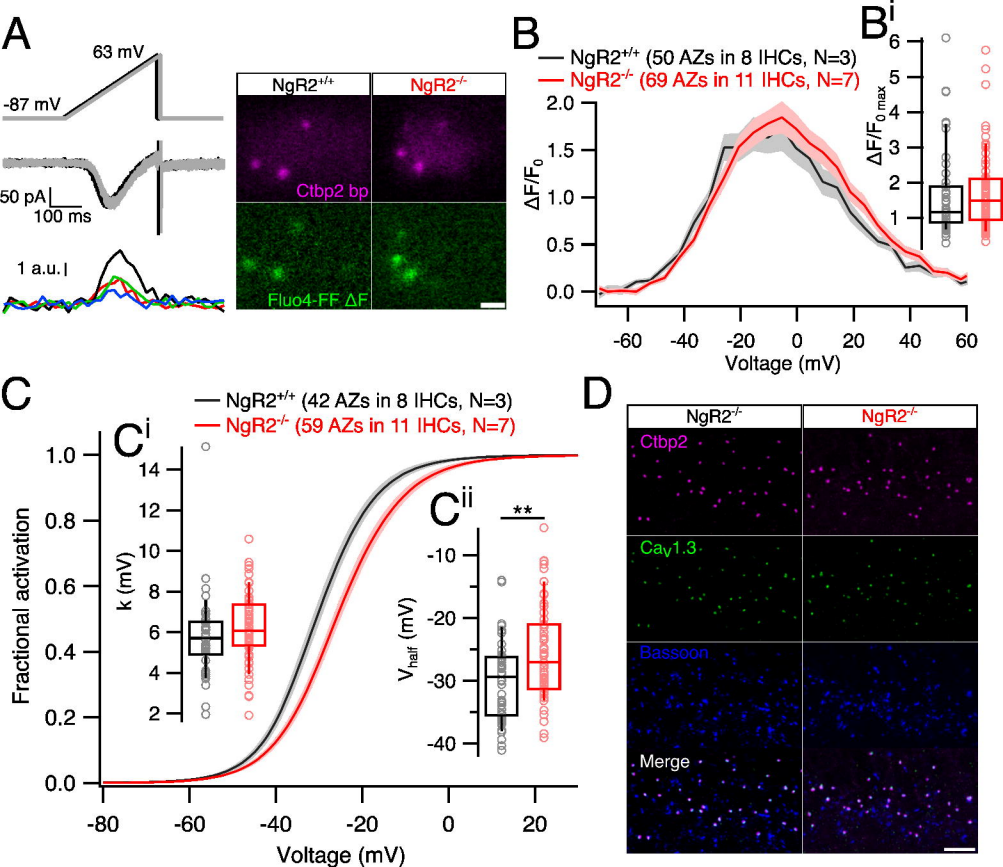
A
63 mV
-87 mV
50 pA
100 ms
1 a.u.
NgR2+/+
NgR2-/-
Ctbp2 bp
Fluo4-FF ΔF
B
NgR2+/+ (50 AZs in 8 IHCs, N=3)
NgR2-/- (69 AZs in 11 IHCs, N=7)
ΔF/F0
Voltage (mV)
Bi
ΔF/F0 max
C
NgR2+/+ (42 AZs in 8 IHCs, N=3)
NgR2-/- (59 AZs in 11 IHCs, N=7)
Fractional activation
Voltage (mV)
Ci
k (mV)
Cii
Vhalf (mV)
**
D
NgR2-/-
NgR2-/-
Ctbp2
CaV1.3
Bassoon
Merge

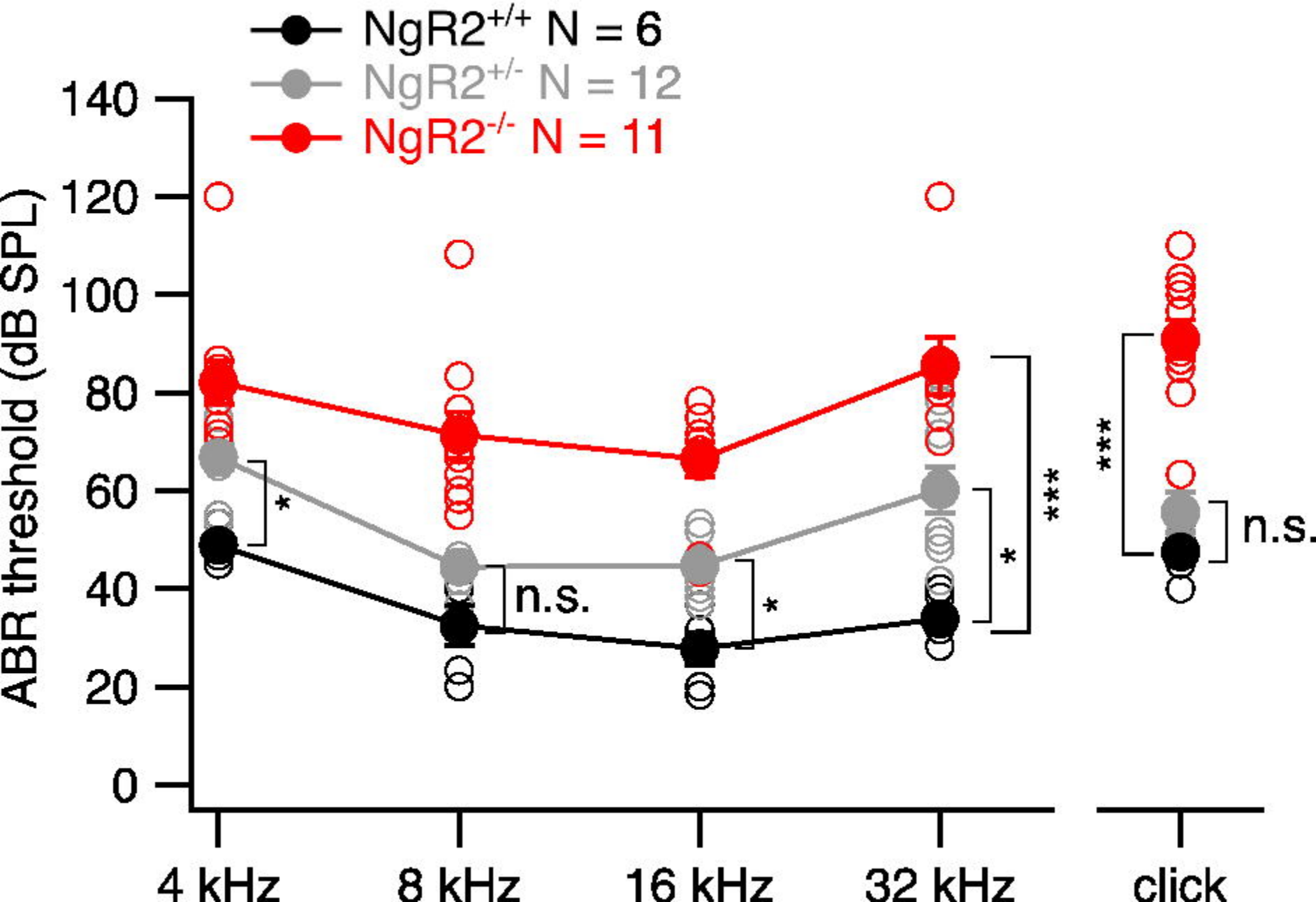
NgR2+/+ N = 6
NgR2+/- N = 12
NgR2-/- N = 11
ABR threshold (dB SPL)
140
120
100
80
60
40
20
0
*
n.s.
*
***
*
***
n.s.
4 kHz
8 kHz
16 kHz
32 kHz
click

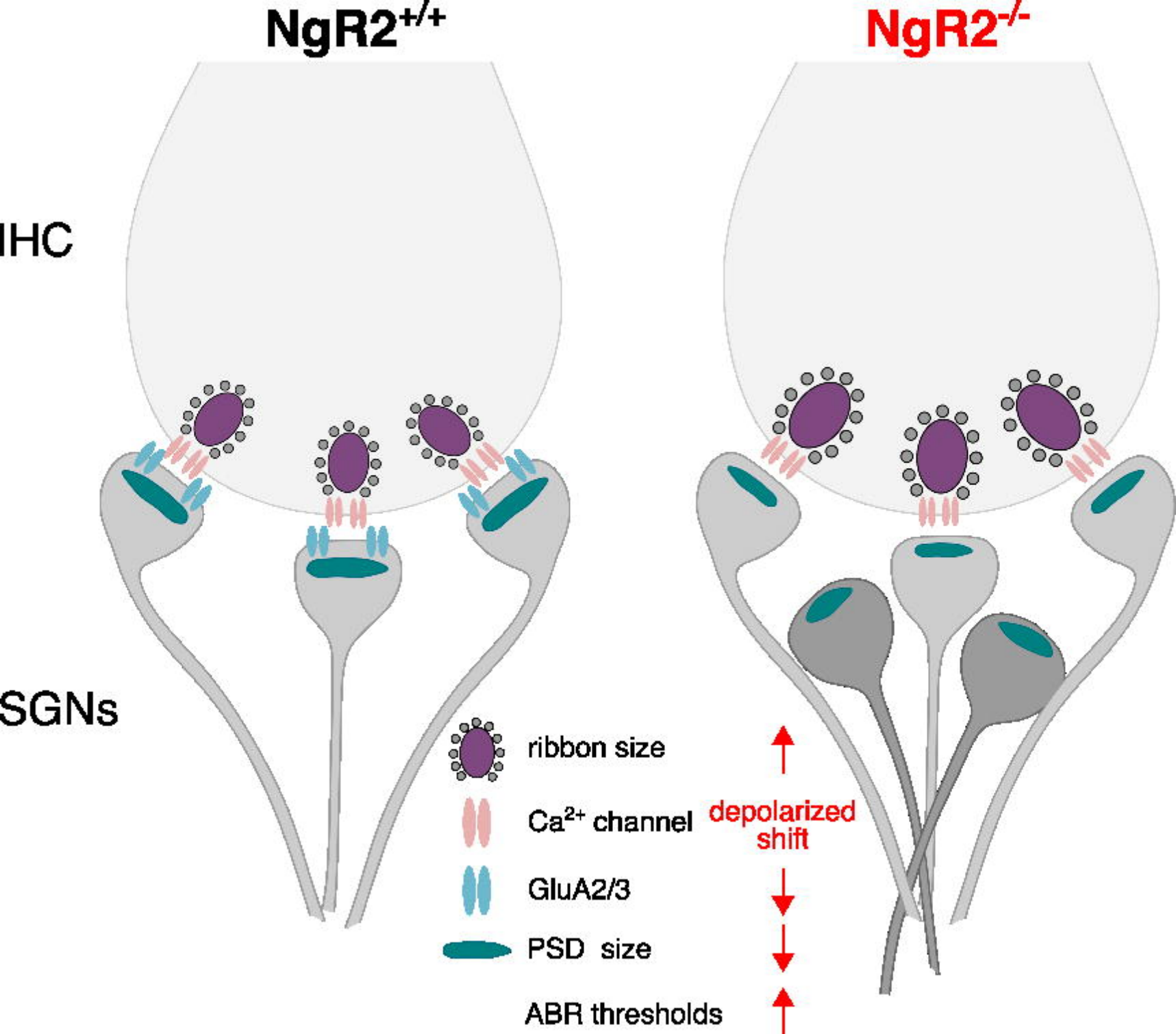
NgR2+/+
NgR2-/-
IHC
SGNs
ribbon size
Ca2+ channel
GluA2/3
PSD size
ABR thresholds
depolarized shift